Microscopic degradation mechanism in formamidinium-cesium lead iodide perovskite solar cells under various stressors intrinsic to operation

Nengxu Li, [1,7] Yanqi Luo, [2,7] Zehua Chen, [3,7] Xiuxiu Niu, [4] Xiao Zhang, [4] Jiuzhou Lu, [4] Rishi Kumar, [2] Junke Jiang, [3] Huifen Liu, [1] Xiao Guo, [1] Barry Lai, [5] Geert Brocks, [3,6] Qi Chen, [4] Shuxia Tao, [3,*] David P. Fenning, [2,*] Huanping Zhou [1,*]

[1] Beijing Key Laboratory for Theory and Technology of Advanced Battery Materials & Key Laboratory of Polymer Chemistry and Physics of Ministry of Education, BIC-ESAT, Department of Materials Science and Engineering, College of Engineering, Peking University, Beijing, P. R. China

[2] Department of Nanoengineering, University of California San Diego, La Jolla, CA 92093, USA

[3] Centre for Computational Energy Research, Department of Applied Physics, Eindhoven University of Technology, P.O. Box 513, 5600MB Eindhoven, The Netherlands

[4] Experimental Centre for Advanced Materials, School of Materials Science and Engineering, Beijing Institute of Technology, Beijing, P. R. China

[5] Advanced Photon Source, Argonne National Laboratory, Lemont, IL 60439, USA

[6] Computational Materials Science, Faculty of Science and Technology and MESA+ Institute for Nanotechnology, University of Twente, P.O. Box 217, 7500 AE Enschede, The Netherlands

[7] These authors contributed equally to this work.

SUMMARY

The most important obstacle to widespread use of perovskite solar cells is their poor stability under environmental stressors. A-site modulation in ABX_3 (methylammonium (MA) free in particular) has proven to be effective in improving the operational stability of the resulting solar cells. Nevertheless, most absorbers still suffer from degradation under operating conditions, the mechanism of which requires investigation. Here, we systematically monitor the evolution of the photovoltaic performance in high-performing formamidinium-cesium lead iodide ($FA_{0.9}Cs_{0.1}PbI_3$) perovskite solar cells for 600 hours, under a controlled environment of stressors intrinsic to operation, such as heat, one-sun illumination, and a stabilized power output (SPO). We find that although $FA_{0.9}Cs_{0.1}PbI_3$-based PSCs exhibit reasonable thermal stability, their stability under illumination or SPO is far behind commercial demands. Synchrotron-based nanoprobe X-ray fluorescence and X-ray beam induced current measurements reveal that current-blocking Cs-rich phases segregate during stress testing. The decrease in performance correlates with the resulting number density of the Cs-rich clusters, and this number density increases in conditions with higher carrier concentration. Modelling based upon density-functional-theory calculations provides evidence for light-generated carriers producing a thermodynamic driving force for such a phase segregation. Our findings provide an effective method to gain insight into determining the relationship between PV performance parameters and micro-scale mechanisms, and shed light on the cation-dependent phase segregation mechanism under operational conditions. It opens a route towards a better understanding of degradation of hybrid perovskite solar cells and guiding the design of more stable materials.

INTRODUCTION

The performance of organic-inorganic halide perovskite solar cells (PSCs) has improved dramatically in the past decade, [1-8] with the highest certified power conversion efficiency (PCE) of 25.2% using a polycrystalline perovskite absorber, [9] which is approaching the state-of-art for crystalline silicon solar cells. However, the poor stability of PSCs in environments of elevated temperature, high humidity, and/or intense irradiation has delayed their commercial deployment. [10-12] Although packaging can extend the stability of PSCs by preventing moisture ingress and reducing evaporation of volatile components in perovskite absorbers upon heating, [13, 14] the stability of PSCs under various stressors is still related to many factors, such as the composition and film quality of perovskites, the selection of charge transport layers and electrodes, as well as the device architectures, etc. [12] Particularly, the continuous operation under intense irradiation for PSCs indicates that improving the illumination and operational stability of perovskites [15, 16] and understanding the degradation mechanisms accounts for the poor stability remains crucial to the effort to harden PSCs for reliable commercial use.

Halide perovskites are generally in the form of ABX_3, where the A-site contains monovalent cations (*i.e.* methylammonium (MA^+), formamidinium (FA^+), and Cs^+), the B-site contains divalent metal ions (Pb^{2+} or Sn^{2+}) and the X-site contains halides (I^-, Br^-, or Cl^-). For illumination and operation-induced degradation pathways, early works have shown that perovskites are easily presented a large amount of Schottky or Frenkel defects, [17, 18] which is mainly attributed to the weak bonding in the crystal [19-21] (such as Pb-I ionic bonds, hydrogen bonds, and Vander Waals interactions) and the soft crystal lattice. [22] Combined with the low energy barrier for ionic migration, [23, 24] halides and organic cations readily migrate through perovskite films, leading to ionic redistribution or even phase segregation upon prolonged testing in the presence of an internal electric field, especially under illumination and/or applied electric load. [25-28] Particularly, phase separation in the hybrid halide (Br and I alloying) system (which can form Br-rich and I-rich phase in perovskites under continuous illumination) have been widely investigated in the $MAPbI_{3-x}Br_x$ perovskites. [28-30] Owing to the obvious bandgap difference between Br-rich and I-rich perovskites (such as, 1.59 eV for $MAPbI_3$ and 2.30 eV for $MAPbBr_3$), the detection method on phase separation of Br-I alloying system is commonly

dependent on photoluminescence characterization. This phase separation in mixed halide perovskites is potentially originated from the localized strain induced by a single photoexcited charge interacting with the soft and ionic perovskite lattice, [31] and the unfavorable formation energies to induce segregation are overcomed by the bandgap reduction of iodide-rich domains. [32] Besides, the thermal instability of MA-containing perovskites makes it unfavourable to be commercial demand absorbers. [33]

Recently, $FA_{1-x}Cs_xPbI_3$ (FACs) system becomes popular due to its high performance and respectful thermal stability. [34] With the additional constituents such as Br and Rb, the thermal stability of $FA_{1-x}Cs_xPbI_3$ based PSCs is further improved [35, 36] to even pass standard 85 °C/85% relative humidity accelerated testing with encapsulation. [37] Meanwhile, they also exhibit considerable stability either under 1-sun illumination [38, 39] or in maximum power point (MPP) tracking [35, 40] conditions. Although $FA_{1-x}Cs_xPbI_3$ based cells show high thermal stability and gradually increased lifetime under operational condition, the comprehensive understanding on the stability of these PSCs under various stressors is still lacking. Pioneer study done by Schelhas *et al.* shown that the degradation pathway of $FA_{1-x}Cs_xPbI_3$ perovskites was associated with phase segregation into the binary phase during operation within 12 h. [41] However, up to now, there is no systematic monitoring on the photovoltaic performance evolution of the $FA_{1-x}Cs_xPbI_3$-based PSCs under various stressors, as well as a microscopic assessment on the magnitude of phase segregation upon different stressors, which is essential on understanding and evaluating the driving forces behind segregation and whether these or similar perovskite materials show promise for durable photovoltaic operation.

In this study, we systematically monitor the performance of high performing MA-free ($FA_{0.9}Cs_{0.1}PbI_3$) PSCs over 600 hours under various environmental conditions, including dark, heat, illumination, and stabilized power output (SPO, under illumination and fixed electric load). The evolution of the current density-voltage (J-V) as a function of time shows that while $FA_{0.9}Cs_{0.1}PbI_3$ based PSCs exhibit respectable thermal stability, they show considerable performance degradation under illumination and SPO conditions. Materials characterization of the aged perovskite absorbers, using X-ray diffraction (XRD), photoluminescence (PL) and synchrotron based X-ray fluorescence microscopy with nanoscale spatial resolution (nano-XRF), provide evidence for a phase segregation of the original perovskites, where

heterogeneous Cs and FA distributions are identified. Further experiments using *In-situ* XRF/X-ray-beam induced current (XBIC) show the Cs-rich clusters to be photoinactive and current blocking, which is likely the main cause of performance loss in $FA_{0.9}Cs_{0.1}PbI_3$ PSCs. First-principles density functional theory (DFT) calculations suggest a thermodynamic driving force for phase segregation, caused by funnelling of the photo-generated carriers into FA-rich regions under illumination. Our approach, combining macroscopic device tests, microscopic materials characterization and atomistic modelling, provides a powerful tool to thoroughly understand the instability of halide perovskites that are intrinsic to device operation, and opens the possibility for designing new perovskite absorber compositions for the ultimate stable PSCs.

RESULTS AND DISCUSSION

Device performance

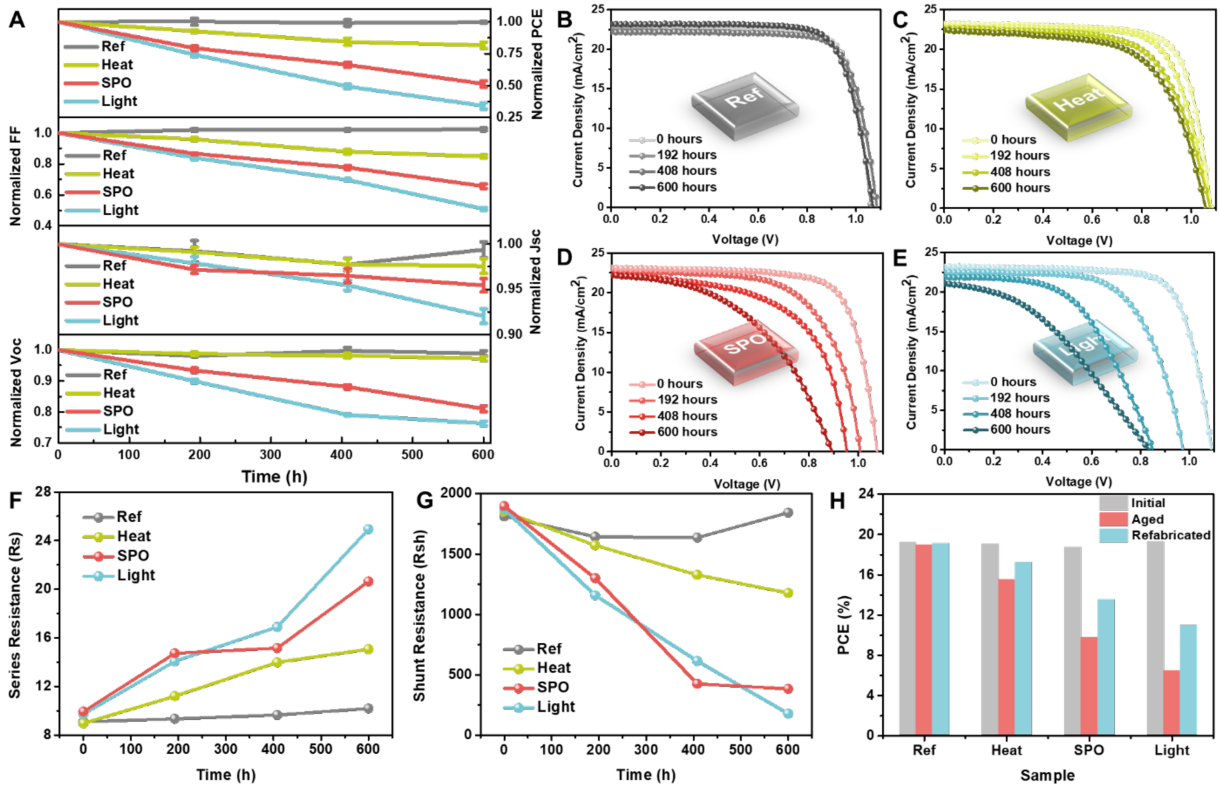

Figure 1. The evolution of photovoltaic performance for perovskite solar cells under different environmental stressors

(A) The evolution of the normalized Voc, Jsc, FF, PCE of PSCs which aged under different environmental stressors. Eight individual devices were tested for each condition with the mean and the standard deviation shown in the plot.

The J-V curves of PSCs after keeping for 0, 192, 408, 600 hours in nitrogen atmosphere (B) at room temperature under dark (ref samples); (C) with 85 °C heating under dark (heat samples); (D) stabilized power output tracking under 1 sun illumination at room temperature (SPO samples); (E) 1 sun illumination at room temperature with open circuit state (light samples).

The extracted series resistance (Rs) and shunt resistance (Rsh) from light J-V curves (*i.e.* Figure 1B-E) are shown in (F) and (G), respectively.

(H) The PCE comparison of initial (no-aged) devices, aged devices, and corresponding refabricated devices under different stressors.

The PSCs used in this work have the conventional n-i-p architecture: ITO/SnO_2/Perovskite/hole transport layer (HTL)/Au, using the composition of $FA_{0.9}Cs_{0.1}PbI_3$ for the perovskite absorber. More details regarding the device architecture and the fabrication procedure are described in the Device Fabrication, Supplemental Information. The statistics of photovoltaic parameters for the freshly made PSCs (Figure S2, Table S1) show an average PCE of 19.16 ± 0.55 %, with the champion device achieving a PCE of 20.12% (Figure S3).

To assess PSCs instability and underlying failure modes under prolonged stressed testing, we monitor device photovoltaic performance over 600 hours of exposure to four distinct stress conditions: 85 ℃ heating in the dark (labelled **Heat**), 1 sun illumination at near room temperature (35 ± 10 ℃) in open circuit condition (labelled **Light**) and a stabilized power output at maximum power point under 1-sun illumination at near room temperature (labelled **SPO**). The reference sample (labelled **Ref**) is stored in the dark at room temperature. Notably, all devices are unencapsulated and maintained in an N_2 environment.

Intermittent J-V measurements (Figure 1A) and average cell parameters (Table S2) shows the evolution of the photovoltaic performance of the devices under Ref, Heat, SPO and Light conditions. Compared with the Ref devices with negligible loss (–1.0 %) after 600 hours, the Heat, SPO, and Light samples all show significant losses in PCE (–18.4 %, –47.7%, and –66.3%, respectively). Except for the Ref samples, Heat caused the slowest PCE decay due to a slight decrease in fill factor (FF). On the other hand, SPO and Light stressors affected device performance considerably, resulting in significant declines in open-circuit voltage (Voc), short-circuit current (Jsc), and FF (Figure 1A). The stability behaviour variation between this study and other recently reported works [35, 37, 40, 42] is likely attributed to the difference in device architecture (n-i-p or p-i-n), absorber composition and film quality (with or without element doping, e.g. Rb, or Br), fabrication method (one or two-step solution process) and interface properties (with or without interface passivation layer), etc. Given the competitive stability of Ref samples in this work, and the systematically evaluated performance under various stressors, our result suggests that the $FA_{0.9}Cs_{0.1}PbI_3$ absorber has good thermal stability but can become unstable under illuminated and SPO conditions.

The photovoltaic performance loss of these devices is further analysed by tracking the evolution of the J-V curves (Figure 1B-E). Series resistance (Rs) and shunt resistance (Rsh) are extracted by fitting the J-V curves (Figure S1B) and their change as a function of stressing time in various stressors is shown in Figure 1F-G. While Rs increases and Rsh decreases in all stressed devices, which are negative on devices performance, the rate and magnitude of the change of these two parameters is larger in Light and SPO samples. The decrease in Rsh, indicative of more shunting paths in a solar cell, reduces the value of Voc and FF, as evidenced in Figure 1A. Variations in Rs and Rsh provide information on system level failure of the layer-

stacked PSC devices, and further characterization is needed to isolate the impact of environmental stressor on the multiple device layers to help understand decay in performance within these devices.

To exclude the impact of stressing conditions on the Au back-contact and HTL (these two layers are known to degrade under accelerated stressing conditions [43, 44]), we re-coated stressed devices with fresh HTL and Au (details are shown in Device Fabrication, Supplemental Information). Refabricated devices display a significant increase in PCE, compared to stressed devices as shown in Figure 1H and Figure S4, which suggests that stressing conditions indeed have a negative impact on the HTL and Au. Note that the PCE does not recover fully in the refabricated samples that are subjected to Heat, Light and SPO, indicating that perovskite absorbers are partially degraded during the aging process and contribute to the remaining performance loss.

In addition, to exclude impact of extrinsic ion migrations, such as Li^+ or Au from the overlaying layers, on degrading absorber performance, [45, 46] we prepared half-cells (ITO/SnO_2/perovskite) and stressed them under Heat and Light stressors (half-cells cannot be aged under SPO due to the incomplete device structure), respectively. After 600 hours of aging, we fabricated them into whole devices by applying the HTL and Au on top, then measured their photovoltaic performance. There are no obvious performance difference between aged half-cell based and refabricated devices under Light and Heat stressing (Figure S5), indicating that mobile additives within the HTL and Au did not affect the perovskite during the aging. Thus we can conclude that the main source of perovskite degradation after aging is the interaction between environmental stressors and the perovskite itself.

Materials characterization

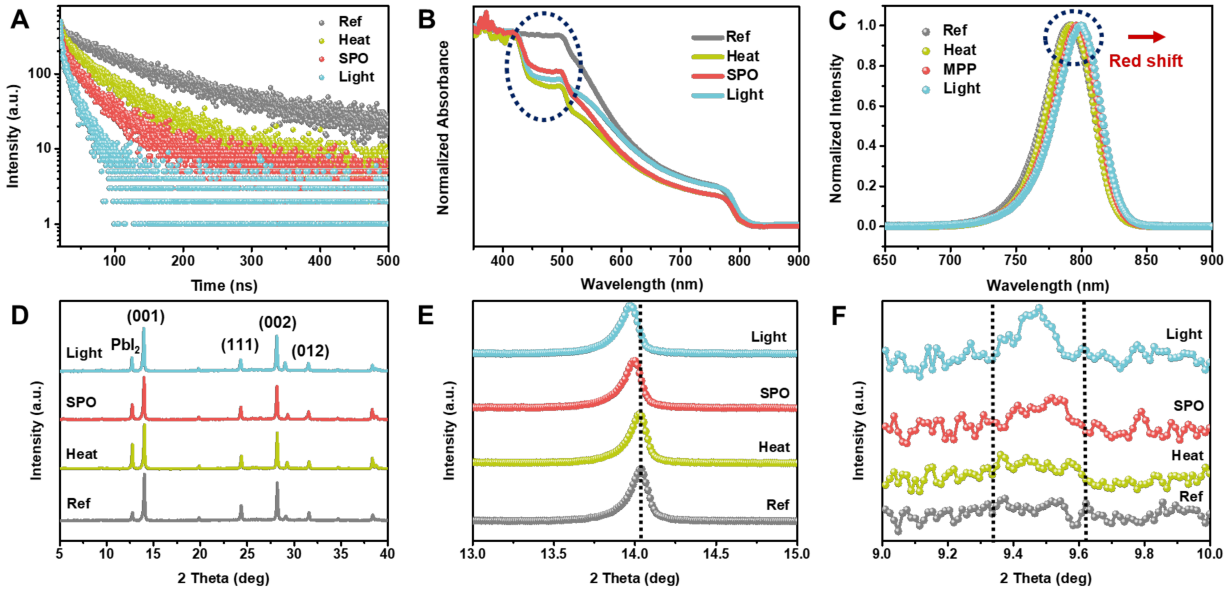

Figure 2. Basic properties of perovskite films obtained from the aged perovskite solar cells under different environmental stressors.

(A) TRPL decay; (B) UV-Vis spectra; (C) Normalized stead-state PL spectra; (D) XRD patterns; (E) Enlarged XRD patterns from 13° to 15°, the peak around 14° represents the (001) lattice plane of $FA_{0.9}Cs_{0.1}PbI_3$; (F) Enlarged XRD patterns from 9° to 10°, the peak around 9.5° represents the δ-phase of $CsPbI_3$.

To gain insights into perovskite degradation under the different environmental stressors, we characterized the optoelectronic, structural and morphological variations in aged perovskite absorbers (which obtained by removing Au electrode and HTL of corresponding PSCs). For comparison, the basic properties of a fresh perovskite film are shown in Figure S6. Time-resolved photoluminescence (TRPL) is used to illustrate carrier lifetime within the stressed samples (Figure 2A and Table S3), where other aged samples have shorter carrier lifetime than Ref with Light being the shortest followed by the SPO and the Heat. The trend in carrier lifetime from TRPL is consistent with the corresponding PSCs performance evolution in Figure 1A.

From UV-vis absorption spectra (Figure 2B), stressed absorbers seem to have similar absorption with Ref in the wavelength range of 550-850 nm. However, a distinct absorption drop in the range of 450-550 nm, is present for all stressed absorbers compared to the Ref sample. We speculate that this absorption loss in aged perovskite films is attributed to the decreased amount of perovskite (which partially decomposed into PbI_2), whereas the PbI_2 itself exhibits much lower molar absorptivity at 500 nm (Figure S7)[47] compared to perovskites, as

also evidenced by XRD (Figure 2D): The aged Ref sample has the least PbI_2 present and almost no absorption drop, while the Heat sample has higher PbI_2 intensity in the XRD pattern with the largest absorption drop in UV-vis absorption spectra among all the stressed samples. Both UV-vis and XRD measurements suggest that Heat has the largest impact on the formation of PbI_2, confirming heating is indeed a primary cause for the decomposition of the perovskites. However, minor decomposition into PbI_2 may not be detrimental (as shown in Figure 2D). The co-existence of PbI_2 has proven to be effective in passivating defects of perovskites [48, 49] and improving the efficiency of PSCs. [50] Thus we consider that the partial decomposition of perovskite in heat-aged samples has no obvious adverse impact on optoelectronic performance of corresponding PSCs.

In addition to PbI_2 formation, the (001) perovskite peak shifts to smaller 2θ for Light and SPO samples compared with Ref and Heat films (Figure 2E), indicating an enlarged lattice spacing. This XRD peak shift seems to be associated with a peak shift in PL emission, where red-shifted emission is observed (Figure 2C). These phenomena may be related to a relative enrichment of FA^+ (large cation, compared with Cs^+) on the A-site of Light and SPO perovskites because FA-rich perovskites have larger crystal lattices as well as smaller band gaps. The formation of such FA-rich phase seems to be accompanied by the formation of the δ-phase $CsPbI_3$, evidenced by a new XRD peak found at about 9.5° in the Light and SPO samples (Figure 2F). Both XRD and PL results suggest that the degradation pathway of the $FA_{0.9}Cs_{0.1}PbI_3$ absorber may be a phase transition from the original stoichiometry to an FA-rich perovskite phase ($FA_{>0.9}Cs_{<0.1}PbI_3$) and an FA-poor perovskite phase ($FA_{<0.9}Cs_{>0.1}PbI_3$), even to the formation of $CsPbI_3$ upon Light and SPO stressed conditions. This is further evidenced by PL mapping (Figure 3A-D), which show a clear spatial heterogeneity in the Light and SPO compared to the Ref and Heat films. If the PL signals of Ref and Heat samples are considered to originate from $FA_{0.9}Cs_{0.1}PbI_3$, then part of the inhomogeneous PL signals of Light and SPO samples may correspond to FA-rich (yellow regions of PL maps) and FA-poor (brown regions of PL maps) perovskites, respectively.

Furthermore, top view scanning electron microscopy (SEM) images give insight into the micromorphology of aged samples (Figure S8 and Supplemental Note 3 in Supplemental Information). As described above, to exclude the influence of HTL and Au on perovskites under

different stressing conditions, the basic properties of aged half-cells (ITO/SnO_2/perovskite) were also characterized (Figure S9 and Table S4). The trend of properties evolution in aged half-cells is similar with aged whole devices (details in Supplemental Note 4 in Supplemental Information), which further exclude the excess effect of HTL and Au on perovskites.

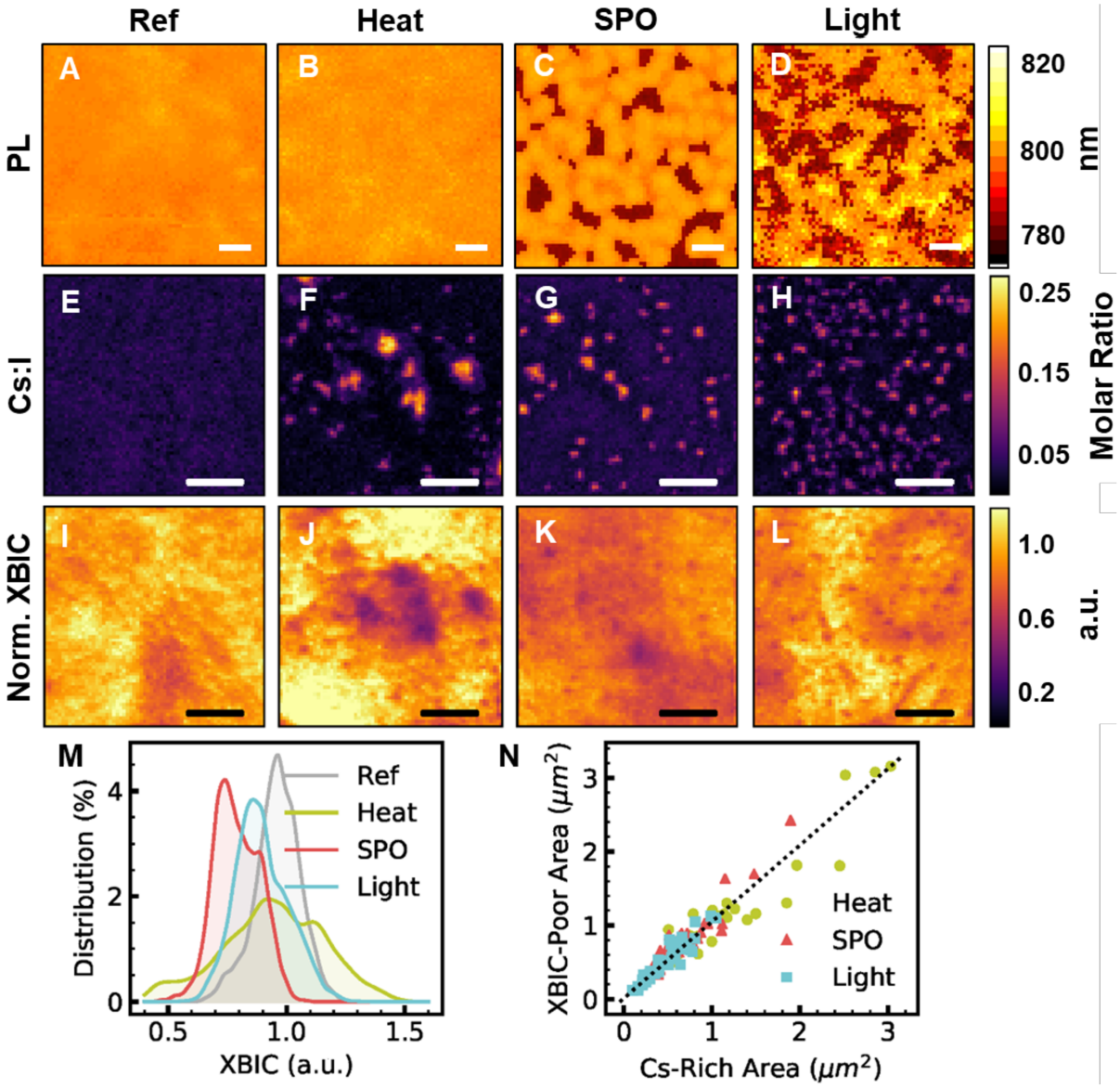

Figure 3. Elemental distribution of Cs and its electronic properties in perovskites devices.

The PL mapping images of perovskite films originated from perovskite solar cells (A-D) and X-ray fluorescence (XRF) mapping of perovskite devices (E-H) that are subjected to Ref, Heat, Light and SPO stressing conditions. The scale bar is 5 µm.

(I-L) X-ray beam induced current (XBIC) mapping of the corresponding regions shown in (E-H). The scale bar is 5 µm.

(M) Pixel-wise frequency distribution of the XBIC current observed in each sample.

(N) Correlation of feature areas as measured by XRF (Cs-rich regions) and XBIC (current-poor regions) in Heat, Light and SPO treated samples.

Nano-XRF is used to study in greater detail the spatial distribution of the film constituents. Fluorescence maps were collected using a focused synchrotron X-ray probe with a 250 nm full-width half maximum (FWHM). The X-ray energy was set at 7 keV to maximize the

measurement sensitivity for I and Cs L-line excitation. The light elements (C, H, N) in the formamidium (FA^+) cation are not observable in the XRF measurement.

The local Cs:I stoichiometry is homogenous within the Ref device, but Cs-rich clusters are observed in all stressed devices (Figure 3E-H). The number density and size of Cs-rich clusters vary across these three stressors. A few large Cs-rich clusters are seen in the Heat sample, while the clusters become increasingly small and numerous in the SPO and Light conditions. The chemical nature of the Cs aggregates is likely to be Cs-rich phase (such as $CsPbI_3$, which is detected in Light and SPO samples as shown in Figure 2F) with the highest Cs:I molar ratio of 0.27, which is almost an order of magnitude higher than the ratio in originally prepared perovskite, where the nominal Cs:I molar ratio is expected to be 0.033 for the $FA_{0.9}Cs_{0.1}PbI_3$ stoichiometry.

To reveal the electronic role of these Cs-clusters, *in-situ* X-ray-beam-induced current (XBIC) was conducted for Ref and stressed devices simultaneously with XRF measurements. The closed correlation between local Cs enrichment and reduced current collection indicates that the Cs-rich clusters observed in the Heat, SPO and Light treated devices suppress charge collection (Figure 3I-L). For example, XBIC poor areas in the centre of Figure 3J are found to align well with the large Cs-rich clusters in the centre of Figure 3F. Similarly, small current suppressing areas in Figure 3K correspond to Cs-rich regions in Figure 3G. The overall effect of the appearance of current suppressing areas is illustrated by histograms of the XBIC signal in each sample shown in Figure 3M. To avoid misinterpretation, the XBIC data shown was corrected to the extent possible for variations in X-ray absorption and subsequent carrier generation due to absorber thickness and morphology variation (Figure S10). This procedure does not remove the effect of morphology fully (*e.g.* variations remain in the relatively homogeneous Ref sample in Figure 3I), likely due to experimental uncertainty of local film thickness and variation of carrier collection probability with film thickness.

We conclude that the Cs-rich clusters are current-blocking and photoinactive. This is determined by performing a cluster analysis and comparing the feature size of XBIC-poor and Cs-rich areas. A correlation plot of the Cs cluster feature sizes as measured by XRF and XBIC is shown in Figure 3N, in which data from all stressed devices is distributed along the guideline

with a slope of 1. The cluster analysis makes explicit the positive correlation and reveals that the XBIC feature size is very close to the size of Cs aggregates in the elemental map.

This microscopic assessment using n-XRF/XBIC of A-site instability in $FA_{0.9}Cs_{0.1}PbI_3$ devices reveals that the stability of the mixed A-site perovskite phase is deteriorated by thermal and optical energy inputs. Interestingly, a high density of Cs-rich clusters nucleate upon continuous light soaking (Light and SPO conditions), while Cs aggregates are larger in size and fewer in number after elevated thermal exposure (85 °C). This finer distribution after illumination compared to the Heat sample suggests that there is a smaller critical nucleus size for nucleation of the Cs-rich phase under illuminated conditions. The temperature difference (between illuminated sample and Heat sample) is not enough to substantially enhance ripening kinetics. [51] On the contrary, illumination is known to enhance ionic conductivity by orders of magnitude. [52] Such enhancements in ion transport would in principle facilitate the illuminated sample reaching high density of nuclei relative to the Heat sample within the same stressing time. The Cs-rich particles are smaller and more numerous in the illuminated sample suggests that a larger energetic driving force exists for phase segregation under illumination than at 85 °C, as in classical nucleation theory the critical radius is inversely related with the thermodynamic driving force. [53]

Mechanism discussion

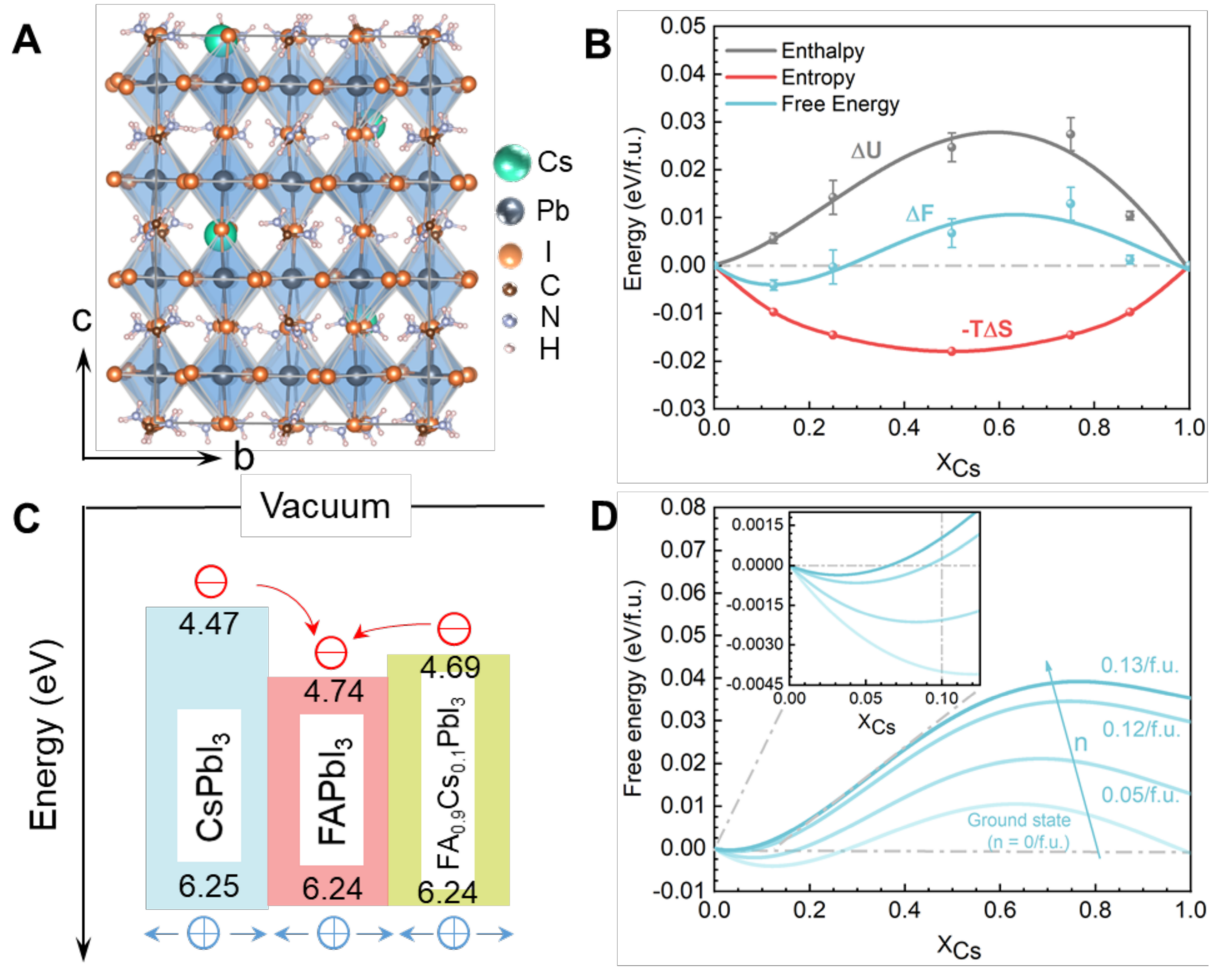

Figure 4. Theoretical analysis of the phase separation mechanism.

(A) Example of a cell of a periodic structure, where 4 out 32 lattice A-sites are occupied by Cs ions, modelling the mixed perovskite $FA_{1-x}Cs_xPbI_3$, with x=1/8.

(B) Calculated enthalpy (ΔU), the entropy contribution ($-T\Delta S$), and free energy (ΔF) of mixing at room temperature (T=300 K) under dark conditions, as a function of x. The symbols are the averaged calculated values, the error bars represent the spread found for different random structures, and the solid lines represent polynomial fits.

(C) Band alignment of $CsPbI_3$, $FAPbI_3$ and $FA_{0.9}Cs_{0.1}PbI_3$, the numbers represent the ionization potentials and electron affinities (in eV). [54]

(D) Calculated free energy curves (ΔF^*) as a function of x, at room temperature (T=300 K), for different photoexcited carrier densities (n). the inset zooms is on the range 0< x <1/8.

The thermodynamic driving force for phase segregation can be identified theoretically, using density functional theory (DFT) calculations. We start by computing the mixing enthalpy $\Delta U(x)$ of $FA_{1-x}Cs_xPbI_3$ perovskites as $\Delta U(x) = U_x - (1-x)U_{FA} - xU_{Cs}$, where U_x, U_{FA}, and U_{Cs} are the energies (per formula unit) of $FA_{1-x}Cs_xPbI_3$, the pure $FAPbI_3$ and $CsPbI_3$ perovskites, respectively. An example of a $FA_{1-x}Cs_xPbI_3$ structure used in the DFT

calculations is shown in Figure 4A. For each composition we have generated a number of structures with FA and Cs cations placed at different random lattice positions. Computational details are given in the DFT Calculations, Supplemental Information.

The calculated $\Delta U(x)$ curve is shown in Figure 4B. Estimating the entropy contribution by the usual mixing entropy expression $\Delta S(x) = -k_B[x \ln x + (1-x)\ln(1-x)]$, then allows for calculating the free energy of mixing $\Delta F(x) = \Delta U(x) - T\Delta S(x)$. The $\Delta F(x)$ curve for T=300 K is also shown in Figure 4B. From this figure it is clearly observed that entropy stabilizes the mixed $FA_{1-x}Cs_xPbI_3$ perovskite for x≤1/4, with a minimum free energy for a composition x~1/8. This result agrees with our experimental findings that $FA_{0.9}Cs_{0.1}PbI_3$ (x=0.1) is stable at room temperature and in dark conditions (see the curves marked "Ref" in Figure 1A, and Figure 3E demonstrates that in the Ref perovskite the Cs ions remain distributed uniformly). Figure 4B also shows that the mixed perovskite becomes unstable for x>1/4, which is consistent with a previous report limiting the amount of Cs that can be incorporated in $FAPbI_3$. [55]

We then model the influence of photoexcitation on possible phase segregation in $FA_{1-x}Cs_xPbI_3$ perovskites [32]. Upon illumination, we assume that pairs of charge carriers are generated uniformly in the material at a density (per formula unit) n. This adds a term $nE_g(x)$ to the energy, where $E_g(x)$ is the band gap of the mixed perovskite (for an expression, see the Band Gap of $FA_{1-x}Cs_xPbI_3$ Perovskites, Supplemental Information). For the unmixed state: (1-x) $FAPbI_3$ + x $CsPbI_3$, we assume that all charge carriers funnel into the compound with the lowest band gap, which in this case is $FAPbI_3$, see Figure 4C. This adds a term $nE_g^{\mathrm{FA}}/(1-x)$ to the total energy of the unmixed state. In summary, under illumination the mixing energy becomes $\Delta U^*(x) = n\left[E_g(x) - E_g^{\mathrm{FA}}\right] + \Delta U(x)$, the last term being the mixing energy under dark conditions, as discussed above.

The mixing free energy $\Delta F^*(x) = \Delta U^*(x) - T\Delta S$, calculated for different values of n, is shown in Figure 4D. Photoexcitation favours phase segregation, essentially because $E_g(x) > E_g^{\mathrm{FA}}$ for all compositions 0< x <1, making it always energetically favourable to collect all charge carriers in a pure $FAPbI_3$ compound. Of course, in order to demix $FA_{1-x}Cs_xPbI_3$ into $FAPbI_3$ and $CsPbI_3$, the mixing entropy (Figure 4B) has to be overcome. Figure 4D shows that

this happens for *n* sufficiently large. Over the whole range 0< x <1, we have an increase of the mixing free energy upon illumination. For *n* sufficiently large the mixing free energy becomes positive over the whole range, indicating that phase separation is favourable at all Cs concentrations. Similarly, for compositions with a higher concentration of Cs, a larger bandgap difference between the $FA_{1-x}Cs_xPbI_3$ alloys and $FAPbI_3$ is expected, which leads to a higher driving force for phase segregation.

The results of this thermodynamic analysis are consistent with the phase segregation under illumination as observed by XRF elemental mapping (Figure 3G-H). The light-treated sample (Figure 3H) shows the largest number density of Cs-rich aggregates. This agrees with the notion that light-generated charge carriers provide a thermodynamic driving force for phase separation. There are fewer Cs-rich aggregates in SPO devices (Figure 3G). We rationalize this by assuming that the average carrier concentration in such devices is lower than that in the light-treated samples, because they are continuously extracted, resulting in a smaller driving force for phase separation.

It should be noted that carrier densities used in these calculations are higher than the typical carrier concentration (~ $10^{16}/cm^3$) under 1 sun illumination (see Free Energy upon Photoexcitation, Supplemental Information for details). [56, 57] The main reason is that in the simple model explained above we have assumed a uniform carrier density, whereas it is highly likely that even in the mixed perovskite $FA_{1-x}Cs_xPbI_3$, charge carriers funnel into statistically FA-rich regions and are concentrated there, before phase separation starts. That this is indeed the case, is indicated by the redshift of PL peak in Figure 2C. Modeling such a non-uniform carrier density is outside the scope of the present paper.

Our focus on the thermodynamics of $FA_{1-x}Cs_xPbI_3$ does not exclude a role for kinetics. Particularly for samples under long-term light soaking, the ion migration kinetics are faster upon illumination than in dark, due to enhanced ionic conductivity and a reduced migration barrier. [58] The fast ion migration kinetics enhance nucleation rate under illumination.

Unlike the illuminated sample, the origin of secondary phase formation in Heat-treated sample (85 °C) seems to be different. We speculate that the large spots of the Cs-rich phase observed in Figure 3F are the products of a thermally induced decomposition. We note that the

calculated decomposition energies (Table S5) of $FAPbI_3$ and $FA_{0.9}Cs_{0.1}PbI_3$ perovskites are markedly smaller than that of the $CsPbI_3$ perovskite.

It should be noted that the most significant performance loss for our FACs PSCs occurred under illumination and operational (SPO) stressors, while the effect of heat on PSC performance (Figure 1A, especially excluding up-layers influence which shown in Figure S4) is comparably small. Generally, it seems that the thermal decomposition of perovskite absorbers can be largely overcome by composition engineering and device encapsulation. Photodecomposition, however, is considered to be a more challenging issue, not only due to the ionic nature of perovskite absorbers, but also the strong interaction between light and perovskites (such as light induced ionic migration and defect formation). Considering that deployed PSCs must operate under continuous irradiation, a deep understanding on the interaction between perovskites and light is required. Cation-dependent phase segregation in FACs perovskites under illumination is evident in the present work. This provides useful guidance to further modify this system to obtain more efficient and stable PSCs. Possible strategies could include, using functionalized additives to enhance the chemical interaction between ions; doping other element (such as Br, Rb, etc.) to change the band structure of perovskites; or modifying the energy levels of the charge transport layers to extract photo-carriers more efficiently. Notably, phase segregation is not the sole reason to cause performance loss of FACs based PSCs, while the cell degradation pathways could be complicated, such as perovskite defects formation, the degradation of other functional layers, bad interfaces contact, ions migration through whole devices, etc. [12] Even so, our work still provides an effective method to gain insight into determining the relationship between PV performance parameters and absorber degradation at a microscopic level. Most importantly, the combination of optoelectronic performance monitoring, advanced characterization, and theoretical analysis can be expanded to other perovskite system upon different ageing conditions, to deepen the understanding of PSCs, as well fabricate the optimum PSCs.

Conclusion

In summary, we have monitored the evolution of photovoltaic performance in MA-free $FA_{0.9}Cs_{0.1}PbI_3$ PSCs aged over 600 hours under stressors intrinsic to PV operation, namely heat, illumination, SPO. Although $FA_{0.9}Cs_{0.1}PbI_3$ based PSCs exhibit reasonable thermal stability, exposure to 1-Sun illumination induces significant degradation over hundreds of hours of operation. We have established that this degradation correlates with a microscopic phase separation, whereby a Cs-rich phase is formed that is photoinactive and current-blocking. Moreover, we have shown that such a phase separation under illumination is to be expected on the thermodynamic driving force originated from light-generated carriers. Our findings provide a microscopic insight to the performance loss of PSCs under stressors typical for operating conditions, which is vital if designing perovskite materials that are better suited for those conditions.

ACKNOWLEDGMENTS

This work was supported by National Natural Science Foundation of China (51722201) (51672008) (51972004) (91733301), National Key Research and Development Program of China Grant No. 2017YFA0206701, Natural Science Foundation of Beijing, China (Grant No. 4182026), Young Talent Thousand Program. The work at UC San Diego was supported in part by the California Energy Commission (EPC-16-050) and the National Science Foundation under Grant No. DMR-1848371. The work at Eindhoven University of Technology, was supported by the Computational Sciences for Energy Research (CSER) tenure track program of Shell and NWO (Project Number 15CST04-2), the Netherlands.

AUTHOR CONTRIBUTIONS

H.Z. and N.L. conceived the idea and designed the experiments. D.P.F., Y.L and R.K. involved in experiment discussion and performed in-situ nano-XRF/XBIC measurements. S.T., G.B. designed and Z.C., J.J. performed the DFT calculations. N.L., X.N., X.Z., C.Z., J.L., C.W., X.G. and H.L. contributed to the fabrication of PSCs. N.L. and X.N. performed UV-vis, XRD, PL, SEM, PL Mapping characterizations. B.L provided beamline support at 2IDD APS for XRF/XBIC measurement. H.Z., D.P.F., S.T., N.L., Y.L. and Z.C. wrote the manuscript. X.N., Q.C., R.K. and G.B. revised the manuscript. All authors were involved in the discussion of data analysis and commented on the manuscript. N.L., Y.L. and Z.C. have contributed equally to this work.

DECLARATION OF INTERESTS

The authors declare no competing interests.

REFERENCES

1. Kojima, A., Teshima, K., Shirai Y., and Miyasaka, T. (2009). Organometal halide perovskites as visible-light sensitizers for photovoltaic cells. J. Am. Chem. Soc. 131, 6050-6051.

2. Kim, H.-S., Lee, C.-R., Im, J.-H., Lee, K.-B., Moehl, T., Marchioro, A., Moon, S.-J., Baker, R. H., Yum, J.-H., Moser, J. E., Grätzel, M., and Park, N.-G. (2012). Lead iodide perovskite sensitized all-solid-state submicron thin film mesoscopic solar cell with efficiency exceeding 9%. Sci. Rep. 2, 591.

3. Snaith, H. J. (2013). Perovskites: The emergence of a new era for low-cost, high-efficiency solar cells. J. Phys. Chem. Lett. 4, 3623-3630.

4. Zhou, H., Chen, Q., Li, G., Luo, S., Song, T., Duan, H.-S., Hong, Z., You, J., Liu, Y., and Yang, Y. (2014). Interface engineering of highly efficient perovskite solar cells. Science 345, 542-546.

5. Yang, W. S., Noh, J. H., Jeon, N. J., Kim, Y. C., Ryu, S., Seo, J., and Seok, S. I. (2015). High-performance photovoltaic perovskite layers fabricated through intramolecular exchange. Science 348, 1234-1237.

6. Yang, W. S., Park, B.-W., Jung, E. H., Jeon, N. J., Kim, Y. C., Lee, D. U., Shin, S. S., Seo, J., Kim, E. K., Noh, J. H., and Seok, S. I. (2017). Iodide management in formamidinium-lead-halide–based perovskite layers for efficient solar cells. Science 356, 1376-1379.

7. Jiang, Q., Zhao, Y., Zhang, X., Yang, X., Chen, Y., Chu, Z., Ye, Q., Li, X., Yin, Z., and You, J. (2019). Surface passivation of perovskite film for efficient solar cells. Nat. Photonics 13, 460-466.

8. Min, H., Kim, M., Lee, S.-U., Kim, H., Kim, G., Choi, K., Lee, J. H. and Seok, S. I. (2019). Efficient, stable solar cells by using inherent bandgap of α-phase formamidinium lead iodide. Science 366, 749-753.

9. NREL National Center for Photovoltaics. (2019). Best research-cell efficiency chart. Available at https://www.nrel.gov/pv/cell-efficiency.html.

10. Leijtens, T., Eperon, G. E., Noel, N. K., Habisreutinger, S. N., Petrozza, A., and Snaith, H. J. (2015). Stability of metal halide perovskite solar cells. Adv. Energy Mater. 5, 1500963.

11. Berhe, T. A., Su, W. N., Chen, C.-H., Pan, C.-J., Chen, J.-H., Chen, H.-M., Tsai, M.-C., Chen, L.-Y., Dubale, A. A., and Hwang, B.-J. (2016). Organometal halide perovskite solar cells: degradation and stability. Energy Environ. Sci. 9, 323-356.

12. Boyd, C. C., Cheacharoen, R., Leijtens, T., and McGehee, M. D. (2019) Understanding degradation mechanisms and improving stability of perovskite photovoltaics. Chem. Rev. 119, 3418−3451.

13. Cheacharoen, R., Boyd, C. C., Burkhard, G. F., Leijtens, T., Raiford, J. A., Bush, K. A., Bent, S. F. and McGehee, M. D. (2018) Encapsulating perovskite solar cells to withstand damp heat and thermal cycling. Sustainable Energy Fuels 2, 2398−2406.

14. Cheacharoen, R., Rolston, N., Harwood, D., Bush, K. A., Dauskardt, R. H. and McGehee, M. D. (2018) Design and understanding of encapsulated perovskite solar cells to withstand temperature cycling. Energy Environ. Sci. 11, 144−150.

15. Islam, M. B., Yanagida, M., Shirai, Y., Nabetani, Y. and Miyano, K. (2019) Highly stable semi-transparent $MAPbI_3$ perovskite solar cells with operational output for 4000 h. Sol. Energy Mater. Sol. Cells, 195, 323-329.

16. Li, N., Tao, S., Chen, Y., Niu, X., Onwudinanti, C. K., Hu, C., Qiu, Z., Xu, Z., Zheng, G., Wang, L., Zhang, Y., Li, L., Liu, H., Lun, Y., Hong, J., Wang, X., Liu, Y., Xie, H., Gao, Y., Bai, Y., Yang, S., Brocks, G., Chen, Q. and Zhou, H. (2019) Cation and anion immobilization through chemical bonding enhancement with fluorides for stable halide perovskite solar cells. Nat. Energy 4, 408-415.

17. Ball, J. M., and Petrozza, A. (2016) Defects in perovskite-halides and their effects in solar cells. Nat. Energy 1, 16149.

18. Kim, J., Lee, S.-H., Lee, J. H. and Hong, K.-H. (2014) The role of intrinsic defects in methylammonium lead iodide perovskite. J. Phys. Chem. Lett. 5, 1312-1317.

19. Motta, C., Mellouhi, F. E., Kais, S., Tabet, N., Alharbi, F., and Sanvito, S. (2015) Revealing the role of organic cations in hybrid halide perovskite $CH_3NH_3PbI_3$. Nat. Commun. 6, 7026.

20. Mellouhi, F. E., Marzouk, A., Bentria, E. T., Rashkeev, S. N., Kais, S., and Alharbi F. H. (2016) Hydrogen bonding and stability of hybrid organic–inorganic perovskites. ChemSusChem 9, 2648-2655.

21. Egger, D. A., and Kronik, L. (2014) Role of dispersive interactions in determining structural properties of organic–inorganic halide perovskites: insights from first-

principles calculations. J. Phys. Chem. Lett. 5, 2728-2733.

22. Jaffe, A., Lin, Y., and Karunadasa, H. I. (2017) Halide perovskites under pressure: accessing new properties through lattice compression. ACS Energy Lett. 2, 1549-1555.

23. Eames, C., Frost, J. M., Barnes, P. R. F., O´Regan, B. C., Walsh, A., and Islam, M. S. (2015) Ionic transport in hybrid lead iodide perovskite solar cells. Nat. Commun. 6, 7497.

24. Azpiroz, J. M., Mosconi, E., Bisquert, J., Angelis, F. D. (2015) Defect migration in methylammonium lead iodide and its role in perovskite solar cell operation. Energy Environ. Sci. 8, 2118-2127.

25. Brivio, F., Caetano, C., and Walsh, A. (2016) Thermodynamic origin of photoinstability in the $CH_3NH_3Pb(I_{1-x}Br_x)_3$ hybrid halide perovskite alloy. J. Phys. Chem. Lett. 7, 1083–1087.

26. Bischak, C. G., Hetherington, C. L., Wu, H., Aloni, S., Ogletree, D. F., Limmer, D. T., and Ginsberg, N. S. (2017) Origin of reversible photoinduced phase separation in hybrid perovskites. Nano Lett. 17, 1028–1033.

27. Yoon, S. J., Draguta, S., Manser, J. S., Sharia, O., Schneider, W. F., Kuno, M., and Kamat, P. V. (2016) Tracking iodide and bromide ion segregation in mixed halide lead perovskite during photoirradiation. ACS Energy Lett. 1, 290–296.

28. Slotcavage, D. J., Karunadasa, H. I., and McGehee, M. D. (2016) Light-induced phase segregation in halide-perovskite absorbers. ACS Energy Lett. 1, 1199–1205.

29. Tang, X., van den Berg, M., Gu, E., Horneber, A., Matt, G. J., Osvet, A., Meixner, A. J., Zhang, D. and Brabec, C. J. (2018) Local observation of phase segregation in mixed-halide perovskite. Nano Lett. 18, 2172-2178.

30. Hoke, E. T., Slotcavage, D. J., Dohner, E. R., Bowring, A. R., Karunadasa, H. I. and McGehee, M. D. (2015) Reversible photo-induced trap formation in mixed-halide hybrid perovskites for photovoltaics. Chem. Sci. 6, 613-617.

31. Bischak, C. G., Hetherington, C. L., Wu, H., Aloni, S., Ogletree, D. F., Limmer, D. T. and Ginsberg, N. S. (2017) Origin of reversible photoinduced phase separation in hybrid perovskites. Nano Lett. 17, 1028-1033.

32. Draguta, S., Sharia, O., Yoon, S. J., Brennan, M. C., Morozov, Y. V., Manser, J. S., Kamat, P. V., Schneider, W. F. and Kuno, M. (2017) Rationalizing the light-induced

phase separation of mixed halide organic–inorganic perovskites. Nat. Commun. 8, 200.

33. Conings, B., Drijkoningen, J., Gauquelin, N., Babayigit, A., D'Haen, J., D'Olieslaeger, L., Ethirajan, A., Verbeeck, J., Manca, J., Mosconi, E., Angelis, F. D., and Boyen, H.-G. (2015) Intrinsic thermal instability of methylammonium lead trihalide perovskite. Adv. Energy Mater. 5, 1500477.

34. Zhou, N., Shen, Y., Zhang, Y., Xu, Z., Zheng, G., Li, L., Chen, Q. and Zhou, H. (2017) CsI Pre-intercalation in the inorganic framework for efficient and stable $FA_{1-x}Cs_xPbI_3$ (Cl) perovskite solar cells. Small, 13, 1700484.

35. Turren-Cruz, S. H., Hagfeldt, A. and Saliba, M. (2018) Methylammonium-free, high-performance, and stable perovskite solar cells on a planar architecture. Science, 362, 449-453.

36. Chen, Y., Yang, Z., Jia, X., Wu, Y., Yuan, N., Ding, J., Zhang, W. H. and Liu, S. (2019) Thermally stable methylammonium-free inverted perovskite solar cells with Zn^{2+} doped $CuGaO_2$ as efficient mesoporous hole-transporting layer. Nano Energy 61, 148-157.

37. Bush, K. A., Palmstrom, A. F., Zhengshan, J. Y., Boccard, M., Cheacharoen, R., Mailoa, J. P., McMeekin, D. P., Hoye, R. L. Z., Bailie, C. D., Leijtens, T., Peters, I. M., Minichetti, M. C., Rolston, N., Prasanna, R., Sofia, S., Harwood, D., Ma, W., Moghadam, F., Snaith, H. J., Buonassisi, T., Holman, Z. C., Bent, S. F. and McGehee, M. D. (2017) 23.6%-efficient monolithic perovskite/silicon tandem solar cells with improved stability. Nat. Energy 2, 17009.

38. Wang, Z., McMeekin, D. P., Sakai, N., van Reenen, S., Wojciechowski, K., Patel, J. B., Johnston, M. B. and Snaith, H. J. (2017). Efficient and air-stable mixed-cation lead mixed‐halide perovskite solar cells with n-doped organic electron extraction layers. Adv. Mater. 29, 1604186.

39. Lee, J.-W., Kim, D.-H., Kim, H.-S., Seo, S.-W., Cho, S. M. and Park, N.-G. (2015) Formamidinium and cesium hybridization for photo- and moisture-stable perovskite solar cell. Adv. Energy Mater. 5, 1501310.

40. Gao, X. X., Luo, W., Zhang, Y., Hu, R., Zhang, B., Züttel, A., Feng, Y. and Nazeeruddin, M. K. (2020) Stable and high-efficiency methylammonium-free perovskite solar cells. Adv. Mater. 32, 1905502.

41. Schelhas, L. T., Li, Z., Christians, J. A., Goyal, A., Kairys, P., Harvey, S. P., Kim, D. H., Stone, K. H., Luther, J. M., Zhu, K., Stevanovic, V. and Berry, J. J. (2019) Insights into operational stability and processing of halide perovskite active layers. Energy Environ.

Sci. 12, 1341-1348.

42. Bi, D., Li, X., Milić, J. V., Kubicki, D. J., Pellet, N., Luo, J., LaGrange, T., Mettraux, P., Emsley, L., Zakeeruddin, S. M. and Grätzel, M. (2018) Multifunctional molecular modulators for perovskite solar cells with over 20% efficiency and high operational stability. Nat. Commun. 9, 4482.

43. Malinauskas, T., Luksiene, D. T., Sens, R., Daskeviciene, M., Send, R., Wonneberger, H., Jankauskas, V., Bruder, I. and Getautis, V. (2015) Enhancing thermal stability and lifetime of solid-state dye-sensitized solar cells via molecular engineering of the hole-transporting material Spiro-OMeTAD. ACS Appl. Mater. Interfaces 7, 11107-11116.

44. Niu, X., Li, N., Zhu, C., Liu, L., Zhao, Y., Ge, Y., Chen, Y., Xu, Z. Lu, Y., Sui, M., Li, Y., Tarasov, A., Goodilin, E. A., Zhou, H. and Chen, Q. (2019) Temporal and spatial pinhole constraints in small-molecule hole transport layers for stable and efficient perovskite photovoltaics. J. Mater. Chem. A 7, 7338-7346.

45. Li, Z., Xiao, C., Yang, Y., Harvey, S. P., Kim, D. H., Christians, J. A., Yang, M., Schulz, P., Nanayakkara, S. U., Jiang, C.-S., Luther, J. M., Berry, J. J., Beard, M. C., Al-Jassim, M. M. and Zhu, K. (2017) Extrinsic ion migration in perovskite solar cells. Energy Environ. Sci. 10, 1234-1242.

46. Domanski, K., Correa-Baena, J.-P., Mine, N., Nazeeruddin, M. K., Abate, A., Saliba, M., Tress, W., Hagfeldt A. and Grätzel, M. (2016) Not all that glitters is gold: metal migration-induced degradation in perovskite solar cells. ACS Nano 10, 6306–6314.

47. Eze, V. O., Lei, B. and Mori, T. (2016) Air-assisted flow and two-step spin-coating for highly efficient $CH_3NH_3PbI_3$ perovskite solar cells. Jpn. J. Appl. Phys. 55, 02BF08.

48. Chen, Q., Zhou, H., Song, T. B., Luo, S., Hong, Z., Duan, H. S., Dou, L., Liu, Y. and Yang, Y. (2014) Controllable self-induced passivation of hybrid lead iodide perovskites toward high performance solar cells. Nano Lett. 14, 4158-4163.

49. Park, B. W., Kedem, N., Kulbak, M., Yang, W. S., Jeon, N. J., Seo, J., Kim, G., Kim, K. J., Shin, T. J., Hodes, G., Cahen, D. and Seok, S. I. (2018) Understanding how excess lead iodide precursor improves halide perovskite solar cell performance. Nat. Commun. 9, 3301.

50. Jiang, Q., Chu, Z., Wang, P., Yang, X., Liu, H., Wang, Y., Yin, Z., Wu, J., Zhang, X. and You, J. (2017) Planar-structure perovskite solar cells with efficiency beyond 21%. Adv.

Mater. 29, 1703852.

51. Futscher, M. H., Lee, J. M., McGovern, L., Muscarella, L. A., Wang, T., Haider, M. I., Fakharuddin, A., Schmidt-Mende, L. and Ehrler, B. (2019) Quantification of ion migration in $CH_3NH_3PbI_3$ perovskite solar cells by transient capacitance measurements. Mater. Horiz. 6, 1497-1503.

52. Kim, G. Y., Senocrate, A., Yang, T. Y., Gregori, G., Grätzel, M. and Maier, J. (2018) Large tunable photoeffect on ion conduction in halide perovskites and implications for photodecomposition. Nat. Mater. 17, 445-449.

53. Balluffi, R. W., Allen, S. M. and Carter, W. C. (2005) Kinetics of materials. John Wiley & Sons.

54. Tao, S., Schmidt, I., Brocks, G., Jiang, J., Tranca, I., Meerholz, K. and Olthof, S. (2019) Absolute energy level positions in tin- and lead-based halide perovskites. Nat. Commun. 10, 2560.

55. Yi, C., Luo, J., Meloni, S. Boziki, A. Ashari-Astani, N., Grätzel, C., Zakeeruddin, S. M., Röthlisberger, U. and Grätzel. M. (2016) Entropic stabilization of mixed A-cation ABX_3 metal halide perovskites for high performance perovskite solar cells. Energy Environ. Sci. 9, 656-662.

56. Johnston, M. B. and Herz, L. M. (2016) Hybrid perovskites for photovoltaics: charge-carrier recombination, diffusion, and radiative efficiencies. Acc. Chem. Res. 49, 146-154.

57. Davies, C. L., Filip, M. R., Patel, J. B., Crothers, T. W., Verdi, C., Wright, A. D., Milot, R. L., Giustino, F., Johnston, M. B. and Herz, L. M. (2018) Bimolecular recombination in methylammonium lead triiodide perovskite is an inverse absorption process. Nat. Commun. 9, 293.

58. Lin, Y., Chen, B., Fang, Y., Zhao, J., Bao, C., Yu, Z., Deng, Y., Rudd, P. N., Yan, Y., Yuan, Y. and Huang, J. (2018) Excess charge-carrier induced instability of hybrid perovskites. Nat. Commun. 9, 4981.

Supplemental Information

Microscopic degradation mechanism in formamidinium-cesium lead iodide perovskite solar cells under various stressors intrinsic to operation

Nengxu Li, [1,7] Yanqi Luo, [2,7] Zehua Chen, [3,7] Xiuxiu Niu, [4] Xiao Zhang, [4] Jiuzhou Lu, [4] Rishi Kumar, [2] Junke Jiang, [3] Huifen Liu, [1] Xiao Guo, [1] Barry Lai, [5] Geert Brocks, [3,6] Qi Chen, [4] Shuxia Tao, [3,*] David P. Fenning, [2,*] Huanping Zhou [1,*]

Experimental Details

Materials SnO_2 colloid precursor (tin(IV) oxide, 15% in H_2O colloidal dispersion) was purchased from Alfa Aesar. PbI_2 (99.999%), CsI (99.9%), N,N-dimethylformamide (99.9%), dimethyl sulfoxide (99.5%), isopropanol (99.5%) and chlorobenzene (99.9%) was purchased from Sigma-Aldrich. Spiro-OMeTAD (99.8%) and PTAA (MOS) was purchased from Xi'an Polymer Light Technology in China. ITO substrate was purchased from Advanced Election Technology Co., Ltd.

FAX (FAI, FACl) were synthesized using the methods reported previously. [1] The details including: 8.8 g formamidine acetate ethanol solution (0.1 mol) was added into a 100 mL three neck flask which immersed in a water-ice bath. A certain amount (0.12 mol) of HX acid was slowly dropped into the bottle with continuous stirring. The mixture was refluxed for 2 hours under N_2 atmosphere. Subsequently, the solution was concentrated to a dry solid by using rotary evaporation at 90 °C. This crude product was re-dissolved into 20 mL ethanol, then 100 μL diethyl ether was slowly dropped along the bottle wall, and white product would deposit. This recrystallization was repeated for three times, and the obtained precipitation was dried in a vacuum oven for 24 hours at 40 °C. The final products were sealed in a N_2 filled glove box for future use.

Device Fabrication. The ITO substrate was cleaned with ultrapure water, acetone, ethanol and isopropanol successively. After 30 minutes of UV-O_3 treatments, SnO_2 nanocrystal solution (2.5%, diluted by water) was spin-coated on the substrate at 4000 rpm for 30 s, then annealed at 150 °C for 30 min in air. The perovskite film was fabricated by a two-step solution process: the PbI_2 (1.3 M, dissolved in DMF:DMSO (9:1, v:v)) mixed with 10% CsI was spin-coated on ITO/SnO_2 at 2300 rpm for 30 s and annealed at 70 °C for 1 min in a nitrogen glovebox. After cooling the PbI_2-coated substrate to room temperature in a nitrogen glovebox, a mixed organic cation solution (FAI 0.35 M; FACl 0.07M, dissolved in isopropanol) was spin-coated with 2000 rpm for 30 s and then annealed at 150 °C for 30 min in air. Then the HTL solution, in which a spiro-OMeTAD/PTAA (36/5 mg mL^{-1}, dissolved in chlorobenzene) mixed solution was employed with the addition of 35 μL Li-TFSI (260 mg mL^{-1}, dissolved in acetonitrile), and 30

μL 4-tertbutylpyridine, was deposited by spin-coating at 1500 rpm for 30 s. The device was finished by thermal evaporation of Au (100 nm) under vacuum.

For refabricated devices mentioned in figure S4, before depositing new HTL and Au layers (same processing as previous) on those aged absorbers, we removed the existing Au electrode with adhesive tape and washed off the HTL with chlorobenzene.

Basic Material Characterization. The morphology of perovskite thin films were measured using a cold field-emission scanning electron microscope equipment (SEM, Hitachi S-4800). The XRD patterns were collected by using a PANalytical X'Pert Pro X-ray powder diffractometer with Cu Kα radiation (λ = 1.54050 Å). Time-resolved photoluminescence (TRPL) was measured by FLS980 (Edinburgh Instruments Ltd) in air (temperature was about 20 ℃, humidity was about 15% RH) with the excitation wavelength at 470 nm, to minimize the photo brightening phenomenon. [2] In addition, the TRPL signal collection time for each sample was controlled at about 30 min, so the results were obtained under a relatively stable state. And all of these samples are measured under same process (same excitation wavelength, same signal collection time) and same environmental conditions, to ensure the comparability of testing results. The UV–vis absorption spectra obtained by an UV–visible diffuse reflectance spectrophotometer (UV–vis DRS, Japan Hitachi UH4150). The current density-voltage characteristics of perovskite devices were obtained using a Keithley 2400 source-measure unit under AM1.5G illumination at 1000 W/m^2 with a Newport Thermal Oriel 91192 1000 W solar simulator.

Detailed Ageing Condition. The **Ref** samples are stored in the dark at averaged temperature about 25 ℃ (temperature is kept in the range of 20-30 ℃); The **Heat** samples are continuously heated at 85 ℃ in the dark; The **Light** samples are aged under continuous 1-sun illumination (white LED source, the spectrum is shown in Figure S1A, light intensity is controlled at 100 mW/cm^2) in open circuit condition at averaged temperature about 35 ℃ (temperature is kept in the range of 25-45 ℃); The **SPO** samples are aged under 1-sun illumination (white LED source, 100 mW/cm^2) with constant 0.9 V bias voltage at averaged temperature about 35 ℃

(temperature is kept in the range of 25-45 ℃). Notably, all devices are unencapsulated and maintained in an N_2 environment for 600 h.

Rsh and Rs calculation. The Rsh is obtained by linear fitting of J-V curve near the Jsc region (getting slope (k_1) of fitted line), then calculating by the formula: $Rsh= -1000/k_1$; the Rs is obtained by linear fitting of J-V curve near the Voc region (getting slope (k_2) of fitted line), then calculating by the formula: $Rs= -1000/k_2$, as shown in Figure S1B.

Nano-XRF Characterization. Functional perovskite solar cells are investigated by means of synchrotron-based nanoproble X-ray fluorescence (n-XRF) with a 250 nm full-width half-maximum (FWHM) focused beam at 7 keV at beamline 2-IDD in a helium environment of the Advanced Photon Source (APS) at Argonne national Laboratory. The *n*-XRF measurement was conducted with the backside Au contact facing the incident X-ray beam, with a full fluorescence spectrum collected point-by-point during mapping. MAPS software was used to fit and deconvolute overlapping peaks and background removal from the fluorescence data. [3] Cs and I XRF signals are quantified using XRF standards purchased from MICROMATTER Tech Inc. Au and Pb signals are quantified using NIST-1832/1833.

***In-situ* n-XRF/XBIC Characterization.** The *in-situ* n-XRF and XBIC (X-ray beam induced current) characterization was conducted using a similar setup as previous studies, [4] where focused X-ray beam penetrates through the backside Au contact, allowing collection of both elemental distribution (n-XRF) and X-ray excited current (XBIC) simultaneously, with 250 nm step size and a dwell time per point of 50 ms. A lock-in amplifier (Stanford Research SR380) and a current pre-amplifier (Stanford Research SR570) at the beamline were used together to collect the induced current signal for XBIC. To acquire a higher signal-to-noise elemental XRF map, a second "elemental" map was collected using a step size as small as 150 nm (oversampling) with dwell time per point of 150 ms.

XBIC Normalization. Film thickness can vary XBIC signal considerably. Given long penetration length of X-ray (> 2 μm, at 7 keV), thicker absorber is likely to absorb more X-ray,

leading larger amount of charge-carrier generation, than thinner sample. Thus, to enable cross sample comparison, we normalized the XBIC maps by the approximated X-ray absorption. X-ray absorption as a function of thickness can be estimated according to Beer Lambert's law, in which absorption of incident flux within a medium is expressed as:

$$I_{X-ray\ absorbed}(t_{film}) = \int_0^{t_{film}} I_0 \exp\left(\frac{-t_{film}}{\lambda_{PSK}}\right) dt_{film} \qquad (1)$$

Where I_0 is the indecent beam flux, λ_{PSK} is the attenuation length of incident X-ray in perovskite (PSK), and t_{film} is the thickness of absorber. Assuming the incident flux can be attenuated by Au current collector overlayer mostly, we can rewrite Eq 1 to account for morphological variation in the overlaying Au layer as below:

$$I_{X-ray\ absorbed}(t_{film}) = \int_0^{t_{film}} I_0 \exp\left(\frac{-t_{Au}}{\lambda_{Au}}\right) \exp\left(\frac{-t_{film}}{\lambda_{PSK}}\right) dt_{film} \qquad (2)$$

In which $t_{Au}\ and\ \lambda_{Au}$ is the thickness and attenuation length of Au layer, respectively. Thickness profiles of both Au and perovskite layers are approximated using similar approach published previously, [5] where the detected elemental concentration in XRF maps were used to scale thickness approximation linearly, with average of elemental counts in XRF matched to nominal thickness of each layer. Film thickness approximation and the corresponding X-ray absorption is shown in Figure S10 Row 1 and Row 2, respectively. According to Eq 2, thin regions (Row 1) have small X-ray absorption (Row 2). The normalized XBIC maps were obtained by dividing raw XBIC with estimated X-ray absorption profiles.

DFT Calculations. To model the mixed-A-cation perovskites $FA_{1-x}Cs_xPbI_3$, we start from a periodic tetragonal supercell containing 32 formula units of $FAPbI_3$ with an initially randomized orientation of FA cations. [6] We then replace FA cations by Cs cations at different concentrations (x=0, 1/8, 1/4, 1/2, 3/4, 7/8, 1). We consider three possible configurations of Cs ions at each concentration. An example of a structure is given in Figure 4A of the main text.

All the calculations are performed using the density functional theory (DFT) approach. We use the projected augmented wave (PAW) method and the GGA/PBE exchange-correlation [7, 8] functional, as implemented in the Vienna ab initio simulation package (VASP). [9] The plane-wave cutoff energy is set at 500 eV and the Brillouin zone is sampled with the Γ point only. An

accuracy of 0.01 meV was adopted for the electronic loops. The shape and volume of the supercell, as well as the atomic positions of each configuration are fully optimized. The convergence criteria on total energy and forces are set at 0.01 meV and 0.02 eV/Å, respectively.

Free Energy. The free energy ($\Delta F(x) = \Delta U(x) - T\Delta S(x)$) of the perovskites $FA_{1-x}Cs_xPbI_3$ is calculated from the mixing energy and entropy. The mixing energy is defined as:

$$\Delta U(x) = U_x - (1-x)U_{\mathrm{FA}} - xU_{\mathrm{Cs}} \qquad (3)$$

Where U_x, U_{FA}, and U_{Cs} are the calculated DFT total energies per formula unit of $FA_{1-x}Cs_xPbI_3$, and the pure $FAPbI_3$ and $CsPbI_3$ perovskites, respectively. We have averaged the energies of all configurations belonging to the same concentration to calculate U_x. We represent the mixing entropy by the usual expression:

$$\Delta S(x) = -k_B[x \ln x + (1-x)\ln(1-x)] \qquad (4)$$

With k_B the Boltzmann constant. The results are shown in Figure 4B of the main text.

Band Gap of $FA_{1-x}Cs_xPbI_3$ Perovskites. The band gap as a function of the Cs concentration x can be estimated as: [6]

$$E_g(x) = (1-x)E_g^{\mathrm{FA}} + xE_g^{\mathrm{Cs}} + 0.12 * x(1-x) \qquad (5)$$

Where E_g^{FA} and E_g^{Cs} are the band gaps of the pure compounds $FAPbI_3$ and $CsPbI_3$, respectively. In a previous combined experimental and computational study, we have established the absolute band edge positions of $FAPbI_3$ and $CsPbI_3$. [10] As the valence band maxima of these two compounds lie at approximately the same position, we may assume that this is also the case for the mixed compounds $FA_{1-x}Cs_xPbI_3$. This means that the absolute position of the conduction band minimum of a mixed perovskites can be estimated from the band gap, Eq. (5), see Figure 4C in the main text.

Free Energy upon Photoexcitation. We estimate the change in the free energy upon photoexcitation as in other report. [11] As in Eqs. (3) and (4), we compare the mixed perovskite $FA_{1-x}Cs_xPbI_3$ with the two pure phases $FAPbI_3$ and $CsPbI_3$. We assume that under illumination of $FA_{1-x}Cs_xPbI_3$, carriers are generated homogeneously in the bulk at a concentration n per

formula unit, so the total energy becomes

$$U_x^* = U_x + nE_g(x) \qquad (6)$$

For the separated phases (1-x) $FAPbI_3$ + x $CsPbI_3$, we assume that all carriers funnel into the low band gap material, which is $FAPbI_3$ in this case. The total energy of photoexcited $FAPbI_3$ then becomes

$$U_{\mathrm{FA}}^* = U_{\mathrm{FA}} + n\frac{1}{1-x}E_g^{\mathrm{FA}} \qquad (7)$$

Using Eqs. (6) and (7) in Eq. (3), with U_x^* and U_{FA}^* replacing U_x and U_{FA} we obtain,

$$\Delta U^*(x) = \Delta U(x) + n\left(E_g(x) - E_g^{\mathrm{FA}}\right) \qquad (8)$$

The free energy of mixing of photoexcited $FA_{1-x}Cs_xPbI_3$ is then given by

$$\Delta F^*(x) = \Delta F(x) + n\left(E_g(x) - E_g^{\mathrm{FA}}\right) \qquad (9)$$

The excitation density n can be estimated as $n = \frac{I*\tau*\alpha}{h\nu} \approx 10^{15}\,\mathrm{cm}^{-3} \approx 10^{-7}$/f.u., where we assume a photon energy $h\nu = 3\ eV$, a light intensity I = 100 mW/cm^2, an absorption coefficient $\alpha = 10^5$ cm^{-1}, and a carrier lifetime τ = 100 ns. [12, 13] Such a carrier density seems far too small to have a marked effect on the free energy balance. However, a long carrier diffusion length and lifetime allow the carriers to accumulate at stochastically-generated low-bandgap regions within $FA_{1-x}Cs_xPbI_3$, perovskite films, i.e., regions with a locally high concentration of FA cations. This funneling of carriers can increase the local carrier concentration to a much higher level. [14]

Supplemental Figures

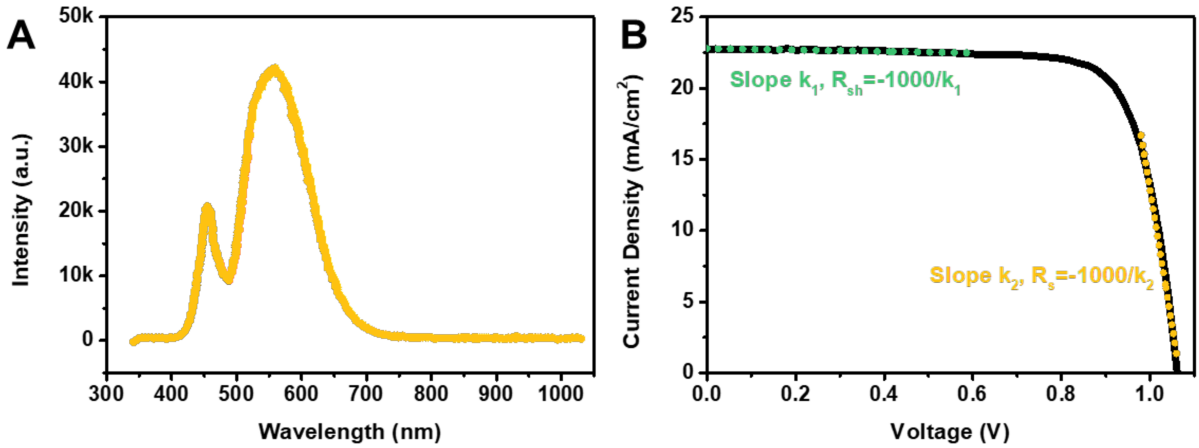

Figure S1 (A) The spectrum of white LED lamp used in this work. (B) The diagram of calculated Rs and Rsh from the J-V curve.

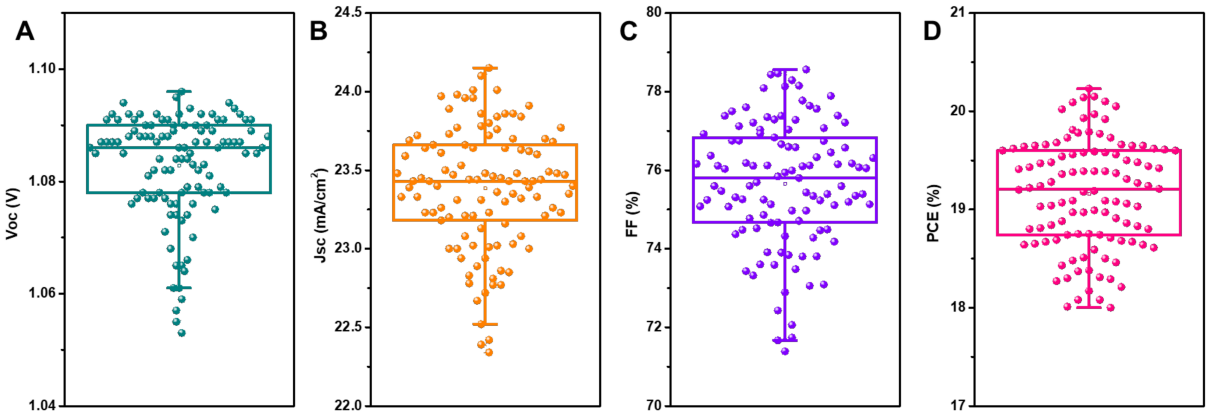

Figure S2 The photovoltaic performance distribution of 109 $FA_{0.9}Cs_{0.1}PbI_3$ based PSCs. (A) Open-circuit voltage (Voc); (B) Short-circuit current (Jsc); (C) Fill factor (FF); (D) Power conversion efficiency (PCE).

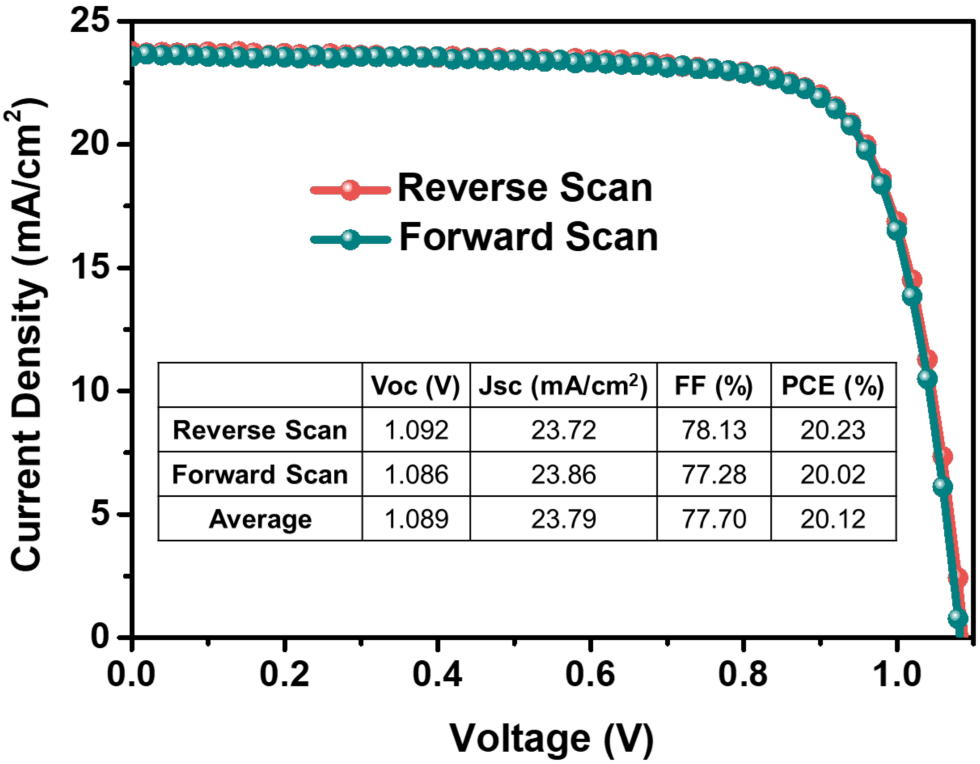

	Voc (V)	Jsc (mA/cm^2)	FF (%)	PCE (%)
Reverse Scan	1.092	23.72	78.13	20.23
Forward Scan	1.086	23.86	77.28	20.02
Average	1.089	23.79	77.70	20.12

Figure S3 Current density-voltage (J–V) curves with reverse (1.2 V to –0.2 V) and forward (–0.2 V to 1.2 V) scan of the best $FA_{0.9}Cs_{0.1}PbI_3$ based PSC device.

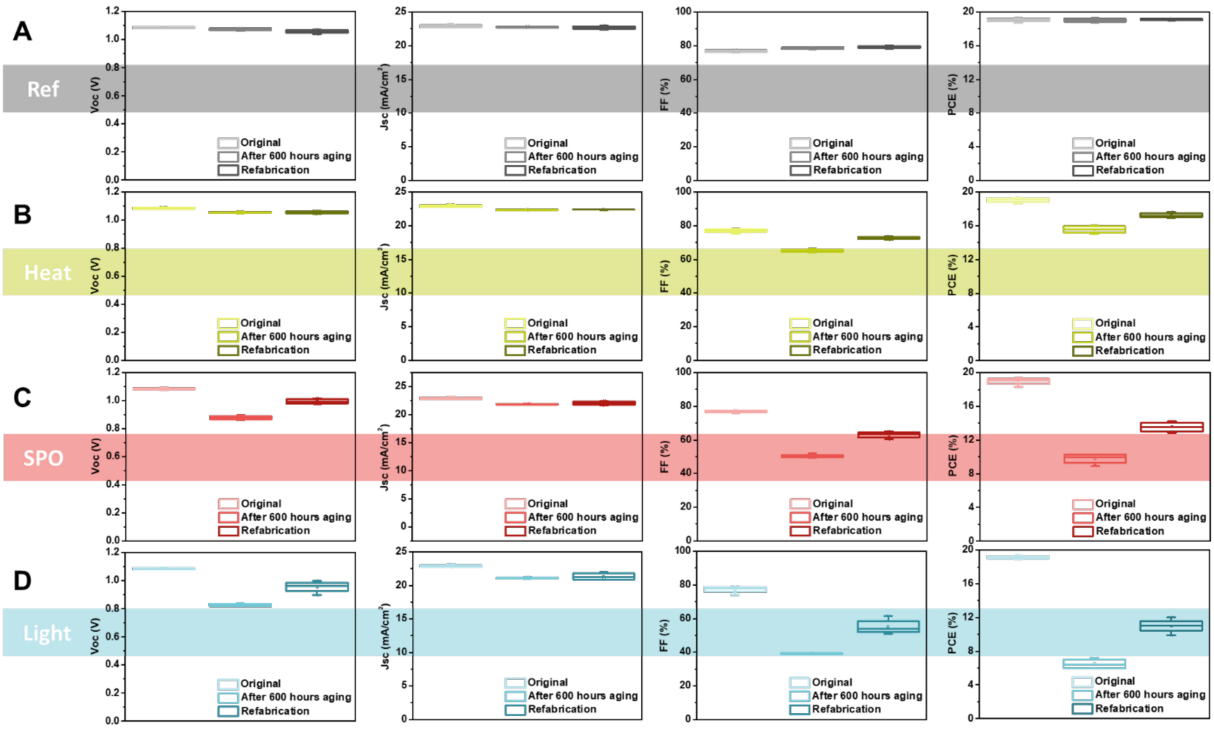

Figure S4 The photovoltaic performance distribution of original devices, aged devices, and refabricated devices which aged under different environmental stressors: (A) Ref devices; (B) Heat devices; (C) SPO devices; (D) Light devices.

Supplemental Note 1: Phase separation in perovskites will lead to Jsc reduction of corresponding PSCs to some extent. This is also proved by our results: the phase separation is obviously discovered in SPO and Light samples (Figure 3), whose Jsc are all decreased compared to their original value. And Light samples exhibit the most serious phase separation (Figure 3) while their Jsc also present the largest drop (Figure 1A). At least, the tendency of Jsc drop is in line with the extent of phase separation. However, in this work, the decrease of Jsc for SPO and Light samples is not significant, where we speculate that there exist two possible reasons:

(1) From the combined characterizations (such as PL mapping and XRF (Figure 3)) we can find that the $FA_{0.9}Cs_{0.1}PbI_3$ perovskite has a phase transition from the original stoichiometry to a FA-rich perovskite phase ($FA_{>0.9}Cs_{<0.1}PbI_3$) and a FA-poor perovskite phase ($FA_{<0.9}Cs_{>0.1}PbI_3$) under stressors, while FA-rich perovskites are photo active while FA-poor perovskites are still weakly photoactive. Given the fact that the bandgap of FA-rich perovskites and FA-poor perovskites don't exhibit too much difference (FA-poor perovskites is below 1.61 eV, FA-rich perovskites of 1.51 eV (speculated from Figure 3A-D)), and the amount of both components

are still small, it is assumed that the light absorption of the film are not seriously affected.
(2) It is possible that the gradient homojunction from FA-poor perovskite (large bandgap) to FA-rich perovskite (small bandgap) existed in phase separated perovskites. Thus, the photo carriers can funnel into FA-rich regions from the FA-poor regions due to their band structure difference. Such a transfer will not lose too much free carriers, therefore, carriers still can flow into external circuit to contribute photocurrent.
Based on above reasons, the discrepancy between the phase separation and the largely preserved Jsc after stressing maybe explained.

Supplemental Note 2: According to Figure S4 & Figure 1H, the photovoltaic parameters (especially PCE) of aged Ref devices after refabrication are similar with those aged Ref samples, indicating that the refabricating process has no remarkable influence on perovskites (either favorable or unfavorable). In addition, it is observed that the obvious performance improvement presented in Heat, SPO and Light samples after refabrication, thus we conclude that the replacement of HTL and Au (HTL and Au electrode are more easily affected by heat, illumination and operation than ref condition) is mainly contributed to partial PCE improvement in refabricated Heat, SPO and Light samples. Even so, the PCE of refabricated PSCs are still lower than the initial value for Heat, Light and SPO samples, respectively, indicating that the degradation of perovskites under various stressors is still an important source for performance loss of PSCs.

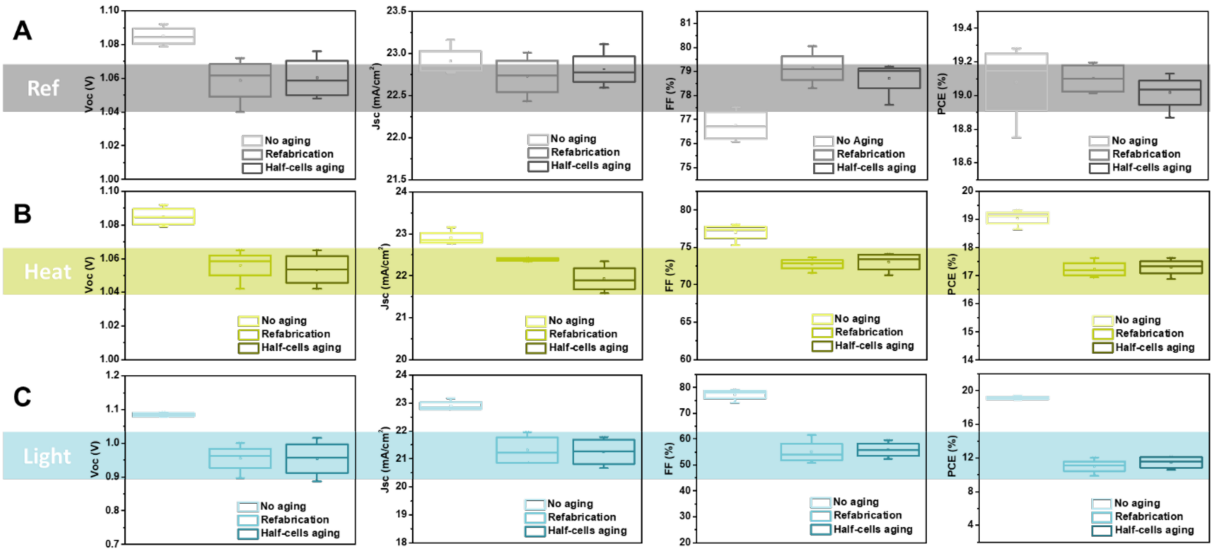

Figure S5 The photovoltaic performance distribution of original devices (No aging), refabricated devices (Refabrication), and devices whose half-cells aged (Half-cells aging) under different environmental stressors: (A) Ref devices; (B) Heat devices; (C) Light devices.

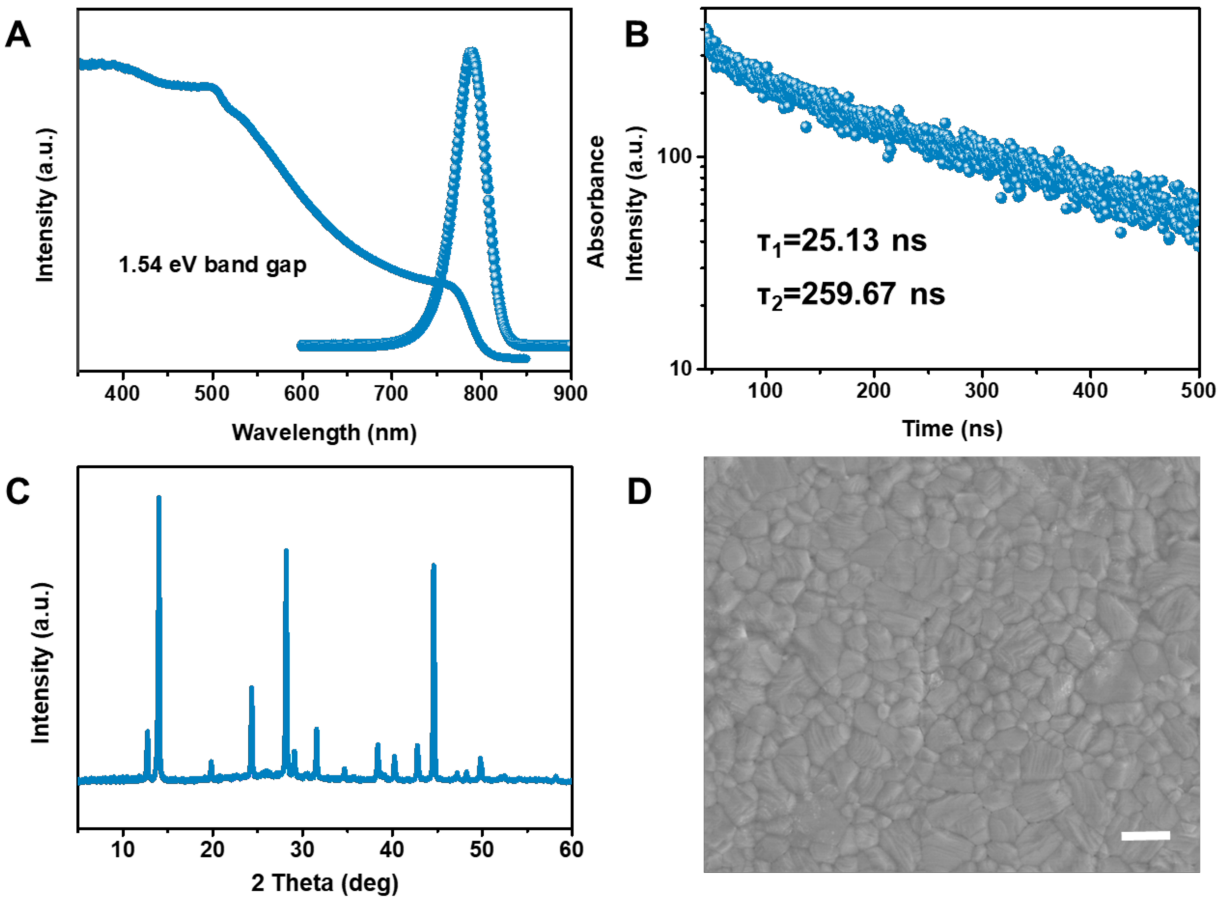

Figure S6 (A) UV-Vis spectra and stead-state PL spectra of no aged perovskite film. (B) TRPL decay of no aged perovskite film. (C) XRD spectra of no aged perovskite film. (D) Top view of SEM images of no aged perovskite film. The scale bar is 1 μm.

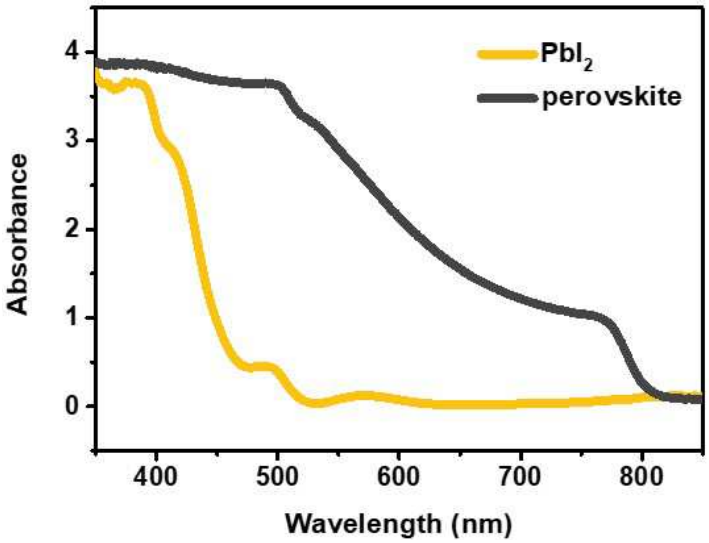

Figure S7 The UV-Vis spectra of pristine PbI_2 film and perovskite film converted from the pristine PbI_2 film.

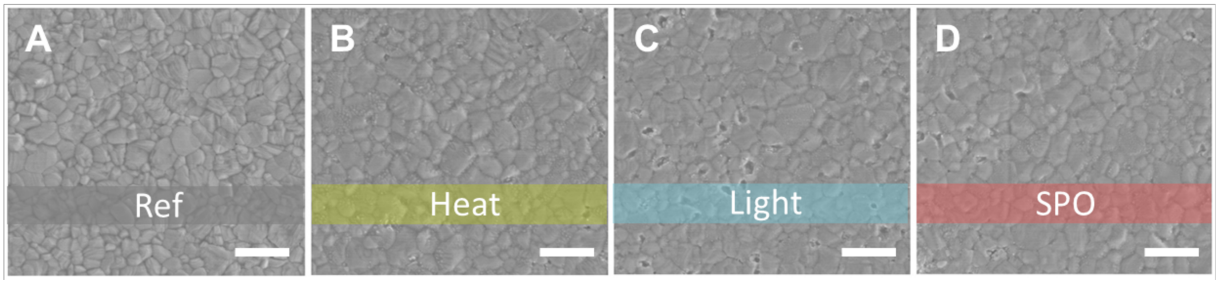

Figure S8 Top view SEM images of perovskite films prepared from perovskite solar cells which aged under different stressors: (A) Ref; (B) Heat; (C) Light; (D) SPO. The scale bar is 2 μm.

Supplemental Note 3: From SEM images there is no obvious grain size difference among these perovskites, however, some pinholes along with grain boundaries (GBs) are occurred in the Light and SPO samples. Considering that phase separation may be related to the ions migration, [15] which is easily happened at the GBs, [16] and the volume of reformed species may also be different from the original species, thus these pinholes may be caused by extensive ions migration and local species redistribution under light.

In addition, the occurred pinholes in Light and SPO stressed films may be correlated with decreased Rsh and reduced PL lifetime in our characterizations. On one hand, the pinholes in perovskite films can provide the direct contact between HTL/Au and ETL/ITO, thus can be served as shunting paths to decrease the Rsh of whole solar devices [17], which is also proved in Figure 1G in revised manuscript. On the other hand, pinholes also can be served as non-radiative recombination centres to reduce the PL lifetime of perovskite films, as evidenced by Figure 2A in this work and other reports [18].

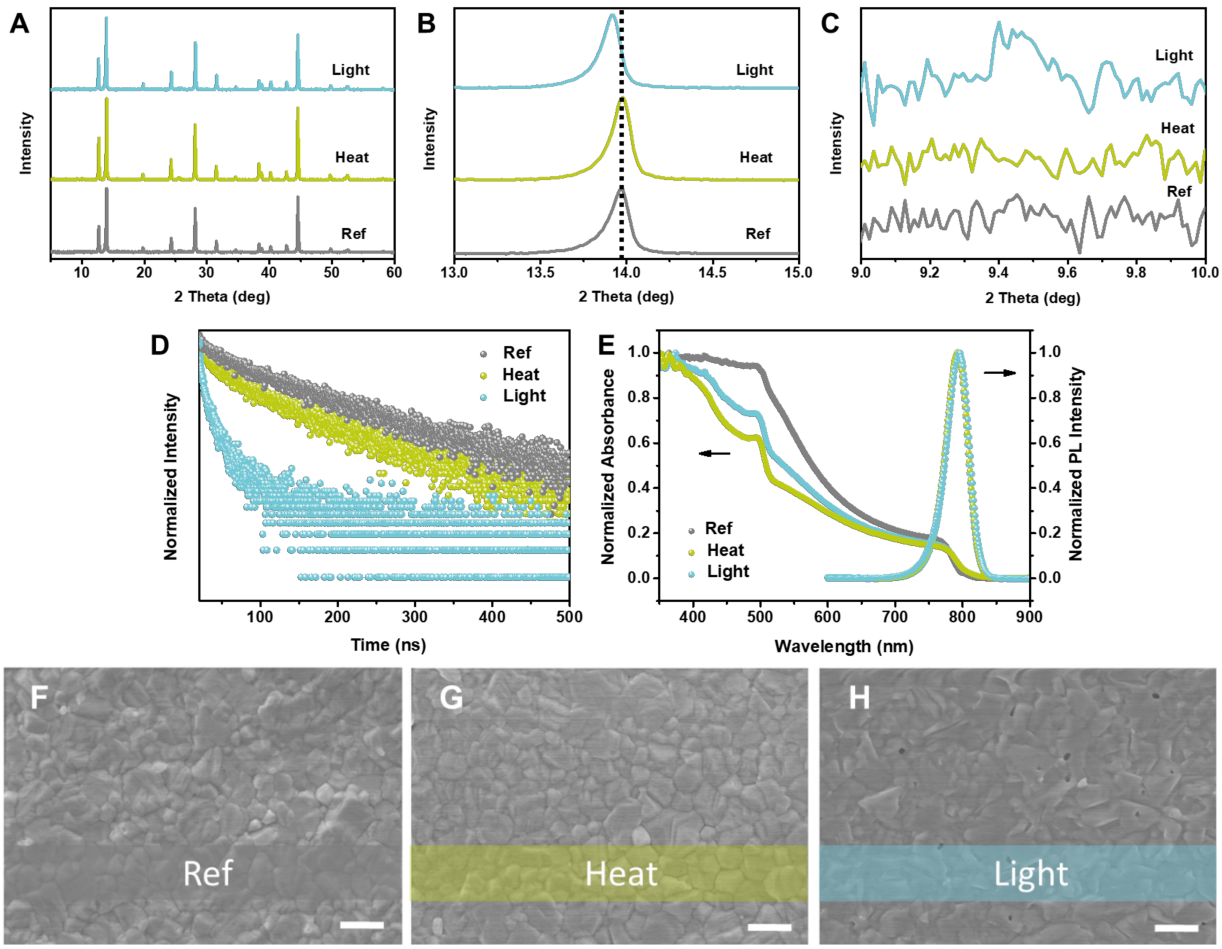

Figure S9 The basic properties of perovskite films which under Ref, Heat, and Light aging conditions for 600 hours: (A) XRD spectra; (B) Enlarged XRD spectra from 13° to 15°; (C) Enlarged XRD spectra from 9° to 10°; (D) TRPL decay; (E) UV-Vis and PL spectra; (F-H) SEM images, the scale bar is 1μm, respectively.

Supplemental Note 4: By comparing the properties of aged half cells (Figure S9) and those aged cells after HTL/Au removal (Figure 2), we can find that although there exist some properties difference between these two type samples, which may be related to the effect of HTL washing process, the overall tendency (such as the PbI_2 content upon perovskite decomposition all follow the tendency: Heat>Light>Ref; the number of pinholes after ageing all follow the tendency: Light>Heat>Ref; the signal of $CsPbI_3$ δ-phase only occurred in Light sample; the 2θ value of (001) lattice plane of $FA_{0.9}Cs_{0.1}PbI_3$ after ageing all follow the tendency: Ref≈Heat>Light, etc.) of perovskite properties under various stressors is similar. From this result we can conclude that the HTL washing process have no obvious influence on basic properties of perovskites films, at least do not change their tendency under various stressors. In

addition, the major characterizations (XRF and XBIC) in this work are conducted using stressed solar cells (without removal of HTL and electrode), so do not need to consider the HTL-washing effect. Based on these discussion, the correlation between micro degradation in perovskites and macro PCE loss in PSCs is still reasonable.

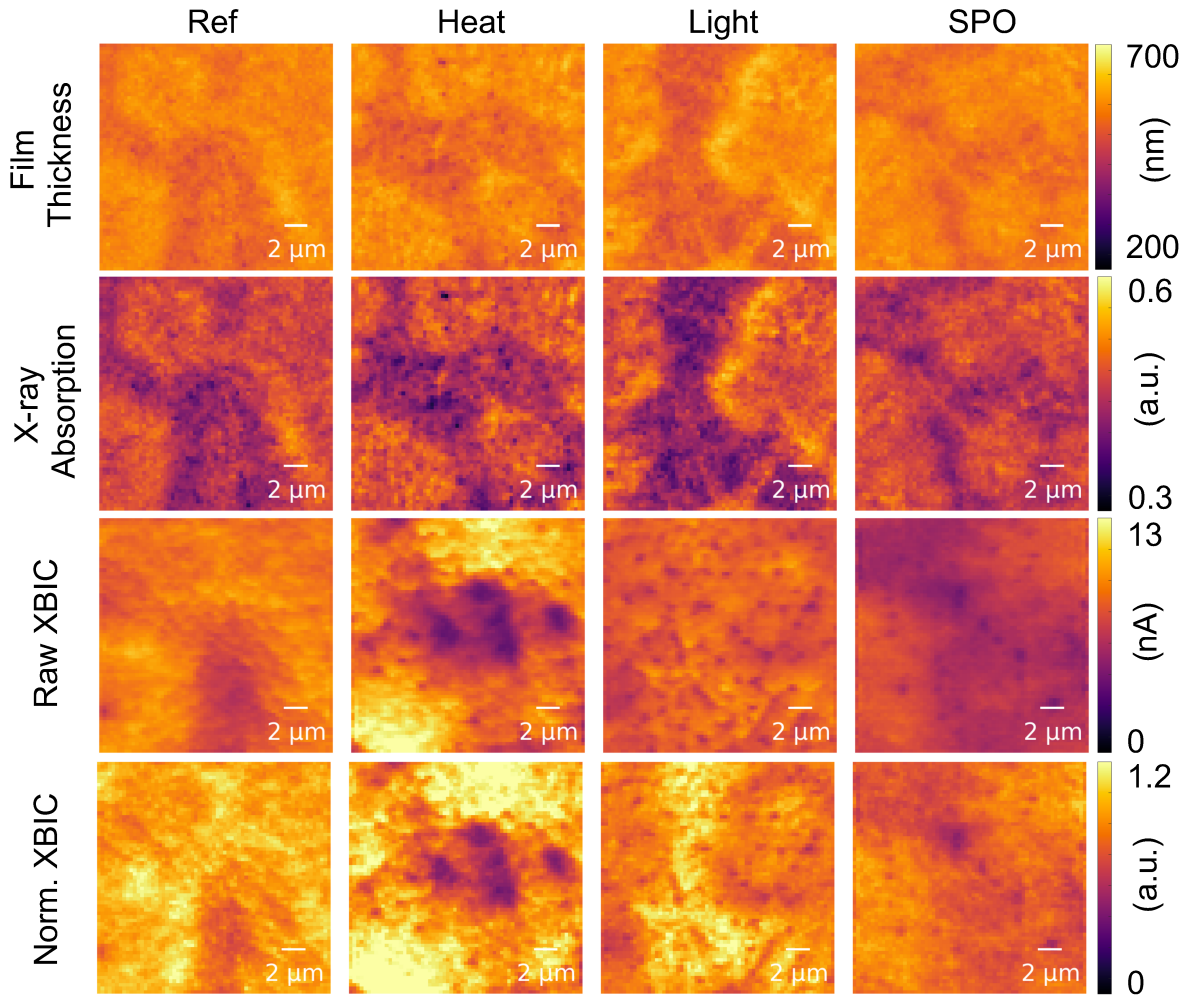

Figure S10. XBIC normalization using approximated X-ray absorption profiles. Perovskite film thickness estimation is shown in Row 1 by scaling average of Pb+I XRF maps to nominal film thickness of 500 nm. Row 2 is the X-ray absorption profiles approximated using Eq 2. Row 3 has the raw XBIC prior to absorption normalization as shown in Row 4.

Supplemental Tables

Table S1 The averaged photovoltaic parameters of 109 $FA_{0.9}Cs_{0.1}PbI_3$ based PSCs.

	Voc (V)	**Jsc (mA/cm^2)**	**FF (%)**	**PCE (%)**
$FA_{0.9}Cs_{0.1}PbI_3$	1.083±0.009	23.38±0.39	75.65±1.59	19.16±0.55

Table S2 The photovoltaic performance evolution of Voc, Jsc, FF, PCE of perovskite solar cells which aged under different aging conditions (each condition contains 8 samples).

		Voc (V)	Jsc (mA/cm^2)	FF (%)	PCE (%)
Ref PSCs	0 hours	1.082±0.005	22.81±0.15	77.50±0.58	19.22±0.20
	192 hours	1.064±0.005	22.73±0.21	78.20±0.43	19.10±0.28
	408 hours	1.082±0.007	22.39±0.16	78.30±0.31	18.91±0.30
	600 hours	1.073±0.008	22.76±0.08	78.55±0.45	19.02±0.19
Heat PSCs	0 hours	1.087±0.003	23.16±0.15	76.07±0.52	19.07±0.22
	192 hours	1.071±0.002	22.71±0.05	73.64±0.79	17.68±0.30
	408 hours	1.065±0.003	22.38±0.03	67.44±0.74	16.08±0.36
	600 hours	1.055±0.004	22.35±0.06	65.16±0.79	15.57±0.39
SPO PSCs	0 hours	1.079±0.004	22.77±0.12	76.31±0.45	18.75±0.15
	192 hours	1.014±0.004	22.26±0.07	66.47±0.44	15.14±0.21
	408 hours	0.956±0.005	22.11±0.05	59.67±0.53	12.66±0.37
	600 hours	0.879±0.013	21.86±0.08	50.34±0.94	9.80±0.55
Light PSCs	0 hours	1.092±0.005	22.89±0.16	77.12±0.75	19.28±0.25
	192 hours	0.976±0.006	22.42±0.08	64.50±0.64	14.15±0.27
	408 hours	0.858±0.006	21.86±0.07	53.51±0.64	9.42±0.40
	600 hours	0.828±0.009	21.08±0.10	39.12±0.46	6.50±0.53

Table S3 The obtained carrier lifetimes of perovskite films originated from perovskite solar cells which under different environmental stressors.

Sample	Lifetime τ_1/ns	Lifetime τ_2/ns
Ref	3.78	102.18
Heat	3.75	57.12
SPO	2.50	39.87
Light	1.61	18.70

Table S4 The obtained carrier lifetimes of perovskite films which under different environmental stressors.

Sample	Lifetime τ_1/ns	Lifetime τ_2/ns
Ref	12.58	129.89
Heat	4.50	85.92
Light	1.48	18.46

Table S5. Decomposition energy (eV) of $FAPbI_3$, $CsPbI_3$ and mixed $Cs_{0.125}FA_{0.875}PbI_3$. The decomposition energy is defined as $\Delta E[A_{1-x}A'_xBX_3] = (1-x)E[AX] + xE\left[A'X\right] + E[BX_2] - E[A_{1-x}A'_xBX_3]$, where $E[Q]$ is the total energy of compound Q.

	$FAPbI_3$	**Orthorhombic $CsPbI_3$**	**δ-$CsPbI_3$**	**$Cs_{0.125}FA_{0.875}PbI_3$**
Decomposition energy (eV)	0.002	0.044	0.110	0.003

Table S6. DFT-optimized lattice parameters and volume of the supercell of each configuration.

	lattice parameter (Å)			angle (°)			volume (Å^3)
	a	b	c	α	β	γ	
x = 0	18.29	18.26	26.07	89.84	90.18	89.80	8708.43
x = 1/8	18.19	18.23	26.04	89.95	90.21	89.85	8633.13
	18.20	18.21	26.03	89.93	90.27	89.82	8628.63
	18.20	18.17	26.04	89.92	90.07	89.97	8615.12
x = 1/4	18.21	18.09	25.98	89.91	90.31	90.07	8555.93
	18.24	18.07	25.88	90.07	90.04	89.88	8534.10
	18.17	18.11	25.99	89.92	90.11	90.04	8552.64
x = 1/2	18.03	17.97	25.95	89.94	90.24	90.23	8411.60
	18.04	18.01	25.74	90.26	90.08	90.19	8363.94
	18.00	18.01	25.94	89.90	90.31	90.13	8408.46
x = 3/4	17.82	17.90	25.94	89.97	89.98	89.71	8276.21
	18.05	18.02	25.42	90.65	89.88	89.84	8267.18
	17.97	18.02	25.50	90.04	91.06	88.89	8255.07
x = 7/8	17.92	17.93	25.37	89.87	91.23	88.51	8150.71
	17.94	17.93	25.36	89.95	91.27	88.68	8155.45
	17.94	17.92	25.38	90.03	91.36	88.58	8154.87
x = 1	17.89	17.86	25.32	90.15	89.09	89.17	8088.59

REFERENCES

1. Li, N., Tao, S., Chen, Y., Niu, X., Onwudinanti, C. K., Hu, C., Qiu, Z., Xu, Z., Zheng, G., Wang, L., Zhang, Y., Li, L., Liu, H., Lun, Y., Hong, J., Wang, X., Liu, Y., Xie, H., Gao, Y., Bai, Y., Yang, S., Brocks, G., Chen, Q. and Zhou, H. (2019) Cation and anion immobilization through chemical bonding enhancement with fluorides for stable halide perovskite solar cells. Nat. Energy 4, 408-415.

2. Quitsch, W. A., deQuilettes, D. W., Pfingsten, O., Schmitz, A., Ognjanovic, S., Jariwala, S., Koch, S., Winterer, M., Ginger, D. S. and Bacher, G. (2018). The role of excitation energy in photobrightening and photodegradation of halide perovskite thin films. J. Phys. Chem. Lett. 9, 2062-2069.

3. Vogt, S. (2003) MAPS: A set of software tools for analysis and visualization of 3D X-ray fluorescence data sets. J. Phys. IV France 104, 635.

4. Baena, J.-P. C., Luo, Y., Brenner, T. M., Snaider, J., Sun, S., Li, X., Jensen, M. A., Hartono, N. T. P., Nienhaus, L., Wieghold, S., Poindexter, J. R., Wang, S., Meng, Y. S., Wang, T., Lai, B., Holt, M. V., Cai, Z., Bawendi, M. G., Huang, L., Buonassisi, T. and Fenning, D. P. (2019) Homogenized halides and alkali cation segregation in alloyed organic-inorganic perovskites. Science 363, 627-631.

5. Luo, Y., Aharon, S., Stuckelberger, M., Magana, E., Lai, B., Bertoni, M. I., Etgar, L. and Fenning, D. P. (2018) The relationship between chemical flexibility and nanoscale charge collection in hybrid halide perovskites. Adv. Funct. Mater. 28, 1706995.

6. Dalpian, G. M., Zhao, X.-G., Kazmerski, L. and Zunger, A. (2019) Formation and composition-dependent properties of alloys of cubic halide perovskites. Chem. Mater. 31, 2497-2506.

7. Perdew, J. P., Burke, K. and Ernzerhof, M. (1996) Generalized gradient approximation made simple. Phys. Rev. Lett. 77, 3865.

8. Blöchl, P. E. (1994) Projector augmented-wave method. Phys. Rev. B 50, 17953.

9. Kresse, G. and Furthmüller, J. (1996) Efficient iterative schemes for ab initio total-energy calculations using a plane-wave basis set. Phys. Rev. B 54, 11169.

10. Tao, S., Schmidt, I., Brocks, G., Jiang, J., Tranca, I., Meerholz, K. and Olthof, S. (2019) Absolute energy level positions in tin- and lead-based halide perovskites. Nat. Commun. 10, 2560.

11. Draguta, S., Sharia, O., Yoon, S. J., Brennan, M. C., Morozov, Y. V., Manser, J. S., Kamat, P. V., Schneider, W. F. and Kuno, M. (2017) Rationalizing the light-induced

phase separation of mixed halide organic–inorganic perovskites. Nat. Commun. 8, 200.

12. DeQuilettes, D. W., Koch, S., Burke, S., Paranji, R. K., Shropshire, A. J., Ziffer, M. E. and Ginger, D. S. (2016) Photoluminescence lifetimes exceeding 8 μs and quantum yields exceeding 30% in hybrid perovskite thin films by ligand passivation. ACS Energy Lett. 1, 438-444.

13. Yamada, Y., Nakamura, T., Endo, M., Wakamiya, A. and Kanemitsu, Y. (2014) Photocarrier recombination dynamics in perovskite $CH_3NH_3PbI_3$ for solar cell applications. J. Am. Chem. Soc. 136, 11610-11613.

14. Stranks, S. D., Eperon, G. E., Grancini, G., Menelaou, C., Alcocer, M. J., Leijtens, T. and Snaith, H. J. (2013) Electron-hole diffusion lengths exceeding 1 micrometer in an organometal trihalide perovskite absorber. Science 342, 341-344.

15. Zhang, H., Fu, X., Tang, Y., Wang, H., Zhang, C., Yu, W. W., Wang, X., Zhang, Y. and Xiao, M. (2019) Phase segregation due to ion migration in all-inorganic mixed-halide perovskite nanocrystals. Nat. Commun. 10, 1088.

16. Shao, Y., Fang, Y., Li, T., Wang, Q., Dong, Q., Deng, Y., Yuan, Y., Wei, H., Wang, M., Gruverman, A., Shield, J. and Huang, J. (2016) Grain boundary dominated ion migration in polycrystalline organic–inorganic halide perovskite films. Energy Environ. Sci. 9, 1752-1759.

17. Kaienburg, P., Hartnagel, P., Pieters, B. E., Yu, J., Grabowski, D., Liu, Z., Haddad, J., Rau, U. and Kirchartz, T. (2018). How contact layers control shunting losses from pinholes in thin-film solar cells. J. Phys. Chem. C 122, 27263-27272.

18. Ge, Q. Q., Ding, J., Liu, J., Ma, J. Y., Chen, Y. X., Gao, X. X., Wan, L. J. and Hu, J. S. (2016). Promoting crystalline grain growth and healing pinholes by water vapor modulated post-annealing for enhancing the efficiency of planar perovskite solar cells. J. Mater. Chem. A 4, 13458-13467.